EUROPEAN ORGANIZATION FOR NUCLEAR RESEARCH.

CERN–EP/99–135
30 August 1999

MAGNETIC PRESSURE AND MECHANICAL CONSIDERATIONS ON A NEW DESIGN FOR THE MAGNETIC HORN FOR THE GRAN SASSO NEUTRINO BEAM

P. Wertelaers

Abstract

In this paper we will discuss design considerations for a new magnetic horn proposed for the neutrino beam to Gran Sasso. The wish to increase considerably the working current of the horn has motivated this study of the development of the forces exerted on the structure as well as the possible deformations and the stresses. Various geometrical imperfections are discussed and analytical treatments are done whenever possible. A full finite element analysis is performed for the highly loaded and geometrically complicated exit region of the horn.

1 INTRODUCTION

A two-stage focusing system is commonly used [1], [2], to focus the charged pions and kaons in the required energy band, into an approximately parallel beam which is directed into a decay channel. Coaxial magnetic lenses, known as the horn and the reflector, are used. Such devices consist mainly of an inner conductor, an outer conductor, current supply and a cooling system. In this paper we will only discuss the properties of the horn. The inner conductor of the horn is basically a slightly conical aluminium tube with two end-caps. This system is subjected to very high currents. The resulting magnetic field gives rise to a net focusing effect for the right-charged particles diverging from the target. Large forces on the structure are produced by the combination of the magnetic flux density and the current. The forces and thereby the material stresses, scale, to first-order calculations, with the square of the applied current. The need to considerably increase the working current of the horn for a proposed new neutrino beam [3], has led to this design report.

A neutrino horn is typically 6 to 7 m long. Figure 1 shows the principle. The current runs axially through the inner conductor, and is returned through the outer conductor. The resulting magnetic field is toroidal, with the classical radial dependence. It rises sharply from zero to maximum value through the inner-conductor wall, decreases in a hyperbolic fashion in the focusing magnetic volume, and drops sharply to zero in the outer-conductor wall. A significant portion of the incident particles will traverse the inner-conductor wall at very small angles. Consequently, it is important that this inner conductor be as thin as possible.

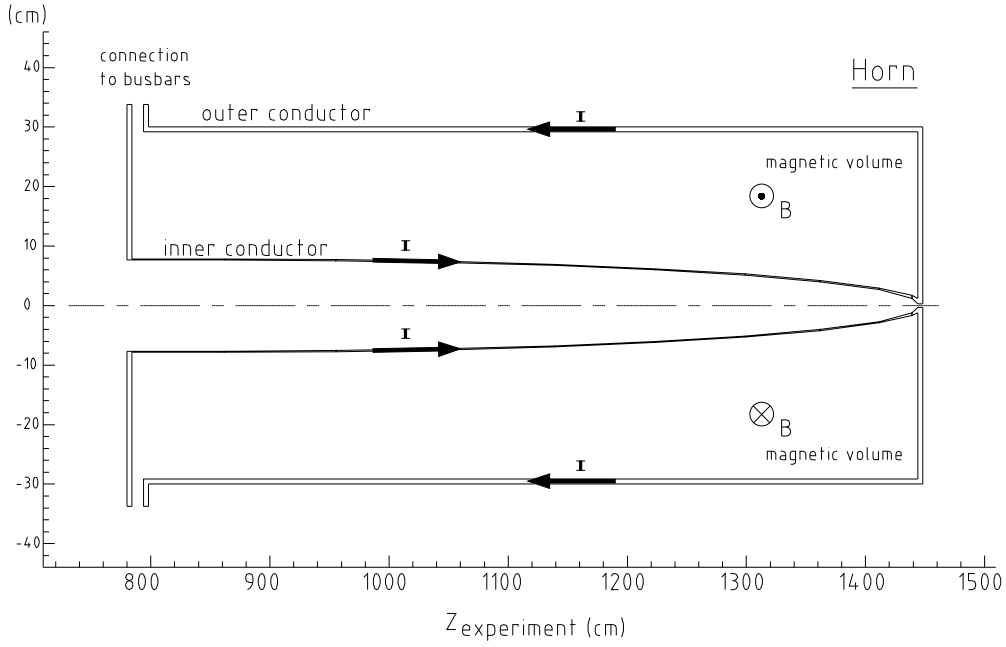

Fig. 1 The principle of a neutrino horn (At regular intervals, a set of ‘cables’, not shown here, centres the inner conductor and bears its weight).

Assumptions and conventions

The term ‘horn’ should be understood in its restrictive sense: the inner conductor.

A cylindrical coordinate system *(r,* θ, *z)* is used by default. As usual, *z* is the beam axis, pointing downstream. The *z* coordinate used here is set to zero where the horn starts, and is thus offset with respect to the experiment's convention (Fig. 1). Our $z = 0$ plane can be retrieved from Fig. 2.

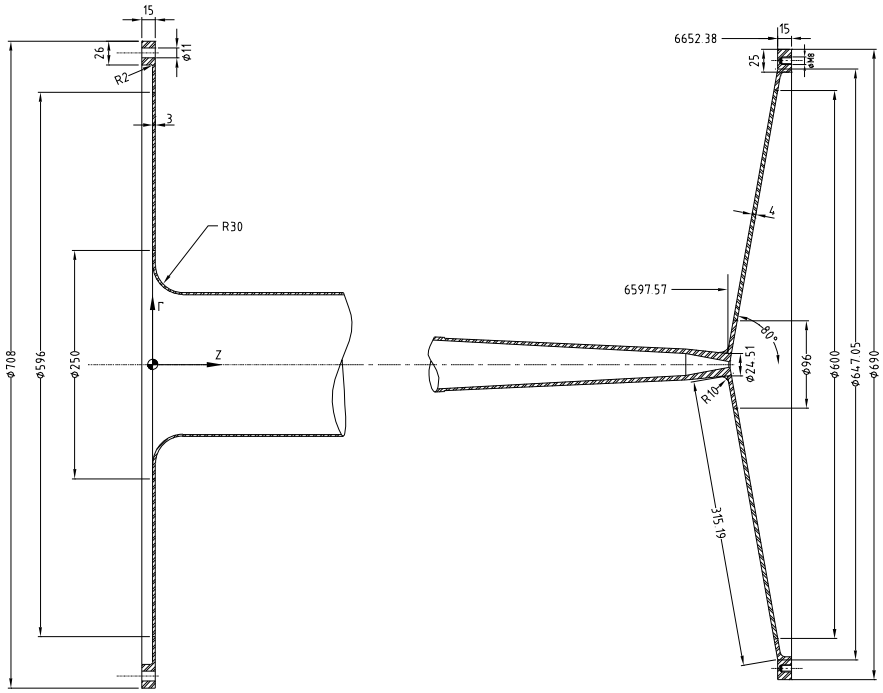

Fig. 2 Present design proposal for the entrance (left) and exit (right) portions of the horn.

Figure 3 defines the relevant terminology for a specific horn cross-section (at a specific *z* location).

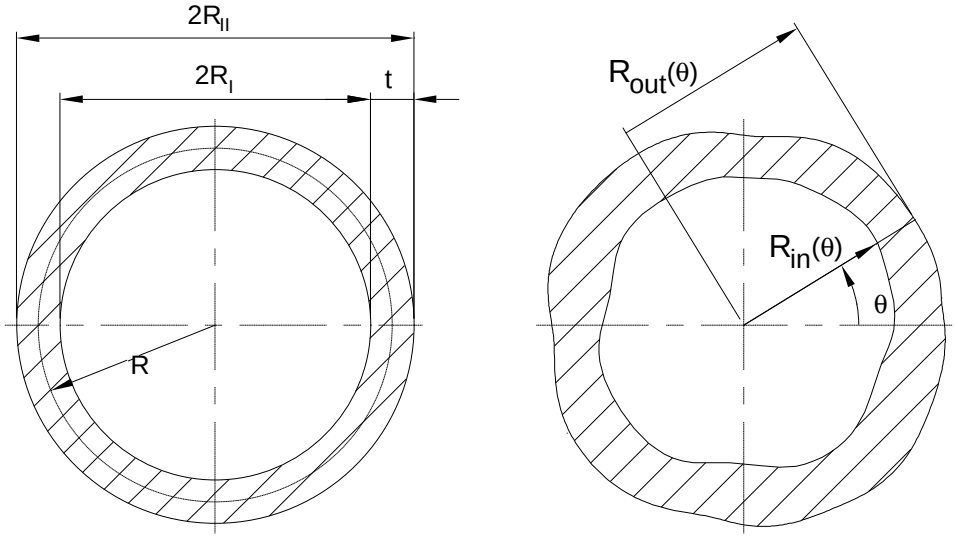

Fig. 3 Geometry definitions: perfect (left) and imperfect (right) cross-sections.

In principle the inner conductor consists of 10 portions. In each portion inner and outer radii vary linearly with z according to Table 1. Numerical results in this report refer to the geometry defined in Fig. 2 and Table 1.

Table 1
The horn geometry

z [mm]	R_I [mm]	R_{II} [mm]	Remarks
0	76.5	78.5	except for transition to end-cap; see Fig. 2
777	76.5	78.5	
1711	75.5	77.5	
2645	72.5	74.5	
3550	67.5	69.5	
4396	60.0	62.0	
5151	51.0	53.0	
5780	40.0	42.0	
6275	27.0	29.0	
6550	12.0	17.0	
6598	3.0	12.0	except for transition to end-cap; see Fig. 2

In reality, the current will only be ‘on’ when really needed, which means it will be pulsed in synchronism with the relevant SPS bursts. The obvious reason is the drive to reduce Joule heat generation. We shall neglect this dynamic property as dynamic effects are beyond the scope of this report. We shall however keep in mind that the total number of pulses, at the end of a successful life, will be of the order of 10^6 to 10^7. Consequently we find ourselves in a fatigue context. The material stress levels will thus be examined with some severity.

Convention: All numerical results quoted in this report are based upon a ‘canonical’ total current of 100 kA. Current densities and magnetic flux densities scale linearly. Mechanical quantities such as force densities, magnetic pressures, reaction forces, stresses, strains and displacements, scale quadratically.

2 ANALYTICAL DEVELOPMENTS FOR THIN-WALLED PORTIONS

In this section we shall make following assumptions.

1) No θ-dependence of the current density.

This is a reasonable assumption, even given that the current will be supplied in only four discrete points on the outer circumference (see Appendix A1). It is even a reasonable assumption in the case of tube imperfections in the form of azimuthal thickness variations: current redistributes inversely proportional to resistance, or, in other words, the electric

equipotential planes will still be orthogonal to the *z* axis. Obviously this implies that we are confident about the homogeneity of the aluminium's resistivity.

2) Thickness *t* small compared to mean radius *R* (Fig. 3).

For relatively thick tubes the notion of 'magnetic pressure' becomes blurred. This issue will be developed below. Furthermore, the relatively simple expressions for strains, stresses, and theoretical buckling pressure lose their validity.

3) Pseudo-negligence of the conical character. For every *z* position we consider an updated cross-section. However, we will develop two-dimensional approaches which implicitly assume a cylindrical geometry.

We propose that the expressions and results from this section be used for the first eight portions (up to $z = 6275$ mm; Table 1). The last two portions necessitate a fully numerical treatment, see Section 3.

Under these assumptions, and considering a perfect geometry, the magnetic field is readily found from Ampère's law. The current density

$$\vec{J} = (J_r, J_\theta, J_z) = (0, 0, J)$$

(hereafter we shall use the notation J for convenience, keeping in mind that it has a sign), results in an integrated total current I (again, in principle, with sign), and with magnetic flux density

$$\vec{B} = (B_r, B_\theta, B_z) = (0, B_\theta, 0)$$

we obtain

$$B_\theta(r) = 0 \qquad \text{for } 0 \le r \le R_I \quad ,$$

$$B_\theta(r) = \frac{\mu_0 \gamma(r)}{r} \qquad \text{for } R_I \le r \le R_{II} \quad ,$$

$$B_\theta(r) = \frac{\mu_0 I}{2\pi r} \qquad \text{for } R_{II} \le r \quad ,$$

where

$$\gamma(r) = \int_{R_I}^{r} J(u)\, u \, \mathrm{d}u$$

and where μ_0 is the free space permeability.

The tube material is assumed to be non-magnetic. Furthermore, there are no Dirac-impulse-like phenomena present in the current density. So $B_\theta(r)$ has to be C^0 continuous (continuity imposed on the function itself, not on its derivatives). This continuity is a trivial consequence of the application of Ampère's law in the above. It will however be explicitly imposed in order to find solutions — with perturbative techniques — to various imperfection models (see Appendices A2, A4 and A5).

The Lorentz force concept yields a volumetric, vectorial force density:

$$\vec{F} = \iiint \vec{J} \times \vec{B} \ \mathrm{dV} \quad (\text{where dV is a volume element}) \ .$$

In the case of our inner tube, this results in a radial force distribution, always inward-pointing.

We will now define a 'magnetic pressure' *p*, with respect to the mean radius *R*.

The force on azimuthal element dθ of the tube is, from Fig. 4 (left),

$$\mathrm{d}\vec{F} = \int_{R_I}^{R_{II}} \vec{J} \times \vec{B} \ r \ \mathrm{d}\theta \ \mathrm{d}r \ \mathrm{d}z$$

and from Fig. 4 (right),

$$\mathrm{d}F = p \ R \ \mathrm{d}\theta \ \mathrm{d}z \ .$$

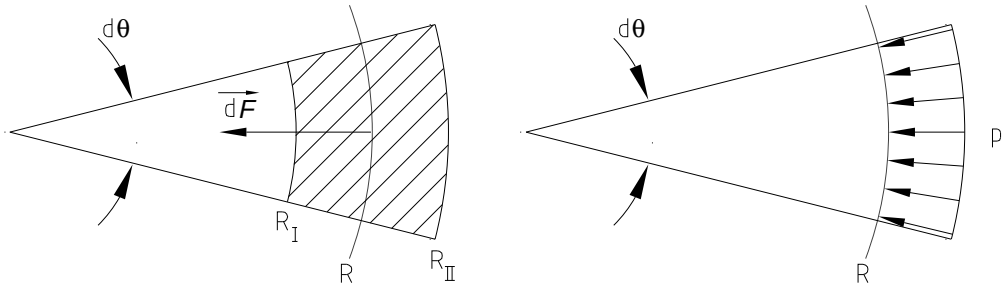

Fig. 4 Our definition of magnetic pressure p.

Confronting these expressions,

$$p = \frac{1}{R} \int_{R_I}^{R_{II}} J \ B_\theta \ r \ \mathrm{d}r = \frac{\mu_0}{R} \int_{R_I}^{R_{II}} J(r) \ \gamma(r) \ \mathrm{d}r \ .$$

In the special case of a (radially) constant *J*, one obtains

$$p = \frac{\mu_0 J^2 R^2 \tau^2}{2} \cdot \left(1 - \frac{\tau}{6}\right) = \frac{\mu_0 I^2}{8\pi^2 R^2} \cdot \left(1 - \frac{\tau}{6}\right)$$

where τ is the thickness ratio:

$$\tau = (t/R) \ .$$

The pressure becomes quasi-independent of the thickness ratio if expressed in terms of total current *I*. Figure 5 indicates when the thickness correction becomes important. The same figure also gives a first impression of the influence of the *J(r)* law. All these corrections are negligible — and hence unnecessary — for the thickness ratios present in the horn's first eight sections. But it should also become apparent that the very extreme exit portion requires a fully numerical treatise of the current density distribution (as well as the magnetic field and the electro-magnetic force distribution).

Figure 6 shows the magnetic pressure, which is obtained with the formula for constant *J*, for the first eight portions.

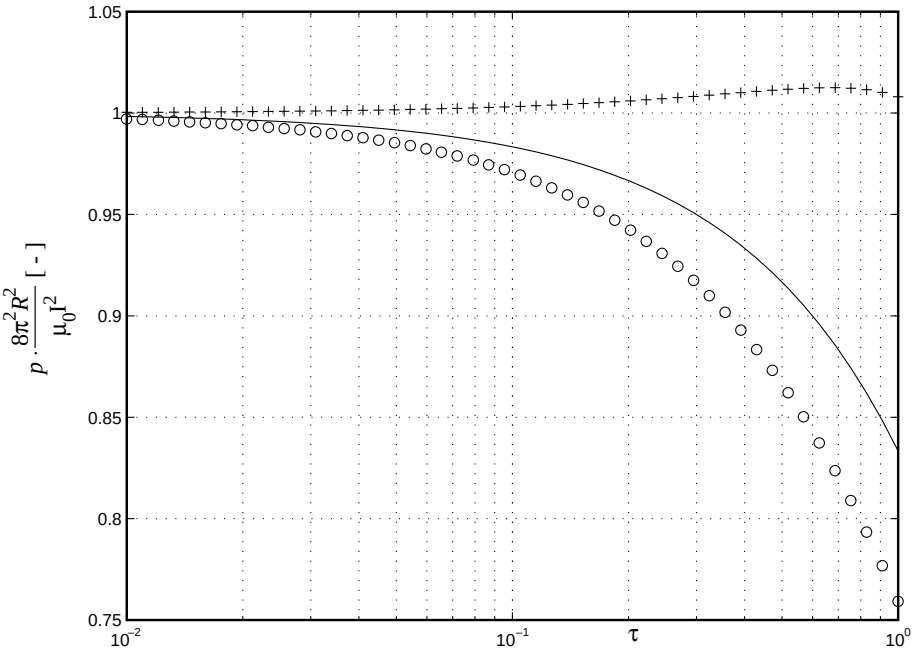

Fig. 5 Correction factor to the magnetic pressure — expressed in terms of total current *I* — as a function of the tube's thickness ratio. Solid line: constant *J*. Dots: linearly increasing *J(r)*, starting from zero value at R_I. Crosses: linearly decreasing *J(r)*, reaching zero at R_{II}.

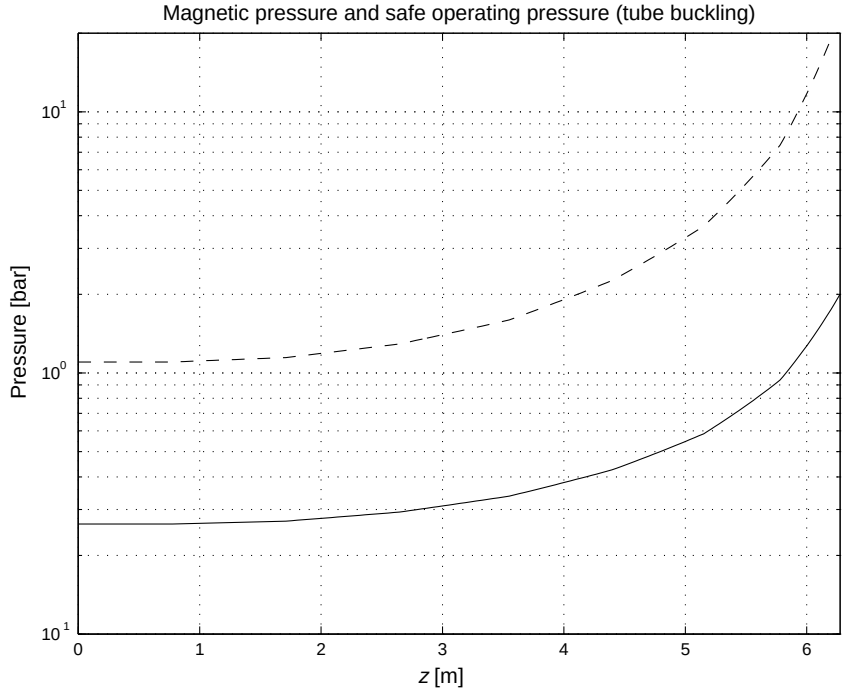

Fig. 6 Magnetic pressure (solid) and assumed allowable pressure (dashed) as a function of *z*.

From the thin-wall pressure vessel formula ($\sigma = -pR/t$) we obtain compressive hoop stresses ranging from 1.0 MPa at $z = 0$, to 2.7 MPa at $z = 6.275$ m.

Ascertaining buckling risks is a difficult issue, especially if we want specific, local information. The following attempt may be disputed by elastic stability insiders.

For a cylindrical tube, a cylindrical vessel of infinite length, the allowable load would be

$$p_{\text{allow}} = \frac{p_{b,\,th}}{S_K} \ ,$$

in which $p_{b,th}$ is the theoretical buckling load:

$$p_{b,\,th} = \frac{E\ \tau^3}{4(1-\nu^2)}$$

where E is the tensile elastic modulus (Young's modulus) and ν Poisson's contraction ratio, taken to be 70 GPa and 0.3, respectively, for aluminium (alloy). The safety factor S_K is taken to be 3, following the spirit of the AD (Arbeitsgemeinschaft Druckbehälter) pressure vessel code. The thickness ratio τ is a function of z, to be taken from Table 1. The result is a profile $p_{\text{allow}}(z)$, shown in Fig. 6, and, as indicated before, subject to some warranty disclaimer.

This treatise of buckling risks may be too pessimistic: In real life, the horn contains end-caps, and is actually somewhat thicker at certain locations. Alternatively, it may be too optimistic: Tube imperfections are normally accounted for in the safety factor S_K. In our electro-magnetic case however, those imperfections may well result in a θ-dependence of p: a complication not treated by the pressure vessel codes. We will try to deal with some aspects of this matter in Appendix A4.

The magnetic pressure decomposes into an axial component, owing to the horn's conical character. The resulting specific axial force is

$$\frac{\mathrm{d}F_z}{\mathrm{d}z} = 2\pi \cdot R(z) \cdot m(z) \cdot p(z)$$

where $m(z)$, the cone's wall slope, is assumed small. This axial loading, shown in Fig. 7, is small and does not really influence the design of the tube itself. The total axial force build-up must however be considered in the design of the end-caps and of the transitions from tube to end-cap, dealt with in Section 3.

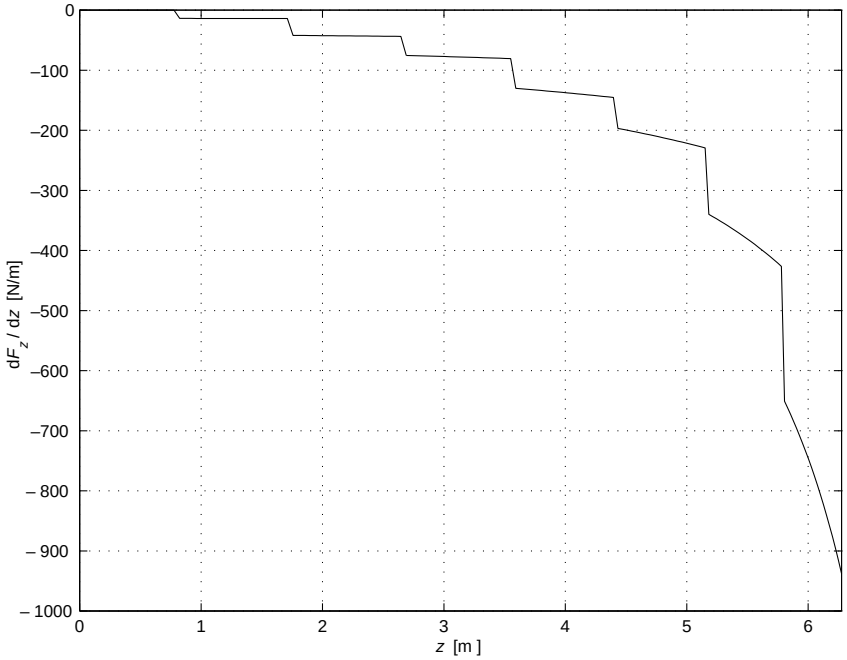

Fig. 7 Axial force per unit length, resulting from magnetic pressure decomposition. Values are for the first eight portions, cumulating to a $F_z = –1010$ N. This force will be a part of the loading input for the mechanical finite element model, dealt with in Section 3.

Lorentz force densities and Maxwell stresses

The Maxwell Stress Tensor formalism is an extremely useful concept to compute forces on bodies in magnetic fields. Its power is that it is applicable not only to impermeable bodies containing free currents, but also to iron, current-free or not, and permanent magnets. In principle it even yields a force distribution on a skin surface, a vectorial stress:

$$\vec{\sigma} = \frac{1}{\mu_0} \cdot \left[(\vec{B} \cdot \vec{n}) \cdot \vec{B} - \frac{1}{2} \cdot |B|^2 \cdot \vec{n} \right] .$$

The *B*-values will be evaluated in ‘air’. In order to interpret the result as true tractions on an iron surface, the *B*-values have to be those in air, approaching in the limit the air/iron interface. The normal $\vec{n}$ refers to the object, and thus points into the air. In the case of eddy-current-free, non-saturated iron, the above condenses approximatively down to a normal surface traction. This results in the well-known simplified formula

$$\sigma_n = \frac{B_n^2}{2\mu_0} .$$

Figure 8 shows the Maxwell stresses in our specific case, where there are no permeable materials.

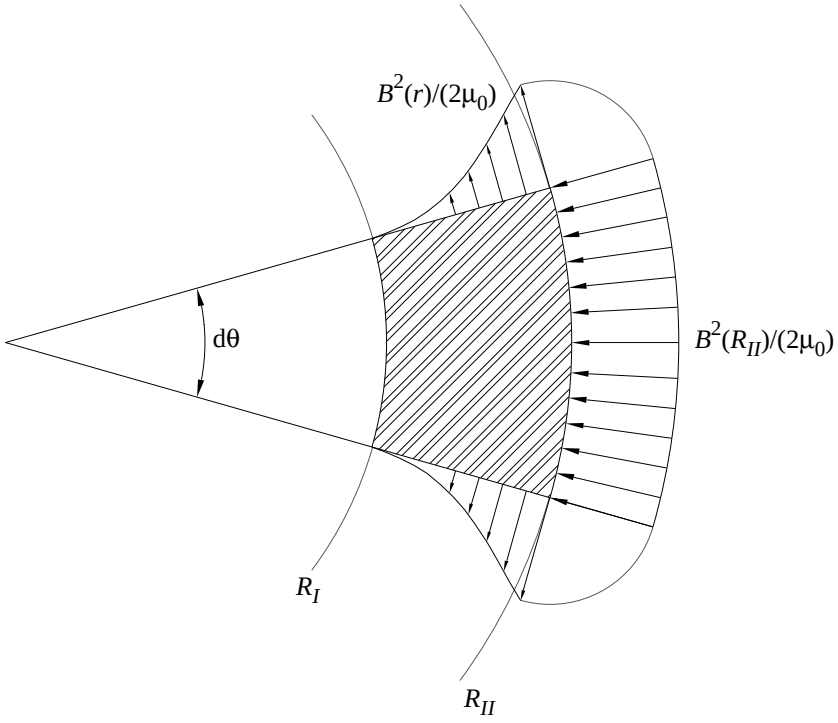

Fig. 8 Normal stresses acting on a tube element dθ, as a result of the magnetic field, obtained with the Maxwell Stress Tensor formalism. Owing to axisymmetry there are no shear stresses.

The total force on the tube element dθ, per unit depth, inward-pointing, is

$$\mathrm{d}F \;=\; \frac{B^2(R_{II})}{2\mu_0}\cdot R_{II}\cdot \mathrm{d}\theta + \mathrm{d}\theta\cdot\int_{R_I}^{R_{II}}\frac{B^2(r)}{2\mu_0}\mathrm{d}r \quad .$$

Consequently, the magnetic pressure is

$$p \;=\; \frac{\mu_0}{2R}\cdot\left[\frac{\gamma^2(R_{II})}{R_{II}} + \int_{R_I}^{R_{II}}\frac{\gamma^2(r)}{r^2}\mathrm{d}r\right] \quad .$$

This should give the same result as the one obtained with the Lorentz force. It can indeed be shown that the following equality holds:

$$2\cdot\int_{R_I}^{R_{II}} J(r)\cdot\gamma(r)\mathrm{d}r \;=\; \frac{\gamma^2(R_{II})}{R_{II}} + \int_{R_I}^{R_{II}}\frac{\gamma^2(r)}{r^2}\mathrm{d}r$$

by integrating in parts the second term of the right-hand side, and observing that

$$\gamma(R_I) \;=\; 0 \qquad \text{and} \qquad \frac{\mathrm{d}\gamma}{\mathrm{d}r} = J(r)\cdot r \quad .$$

Apparently, the Lorentz formulation is the more straightforward one in our specific case. This holds especially in a numerical context, such as finite elements, where the numerical

sensitivities inherent to the Maxwell stress formulation might be of concern. The Lorentz formulation will be exclusively used here.

Misalignment of inner conductor

Of interest is the issue of the net force, in *x*, on the inner conductor, as a result of a misalignment in *x*; see Fig. 9.

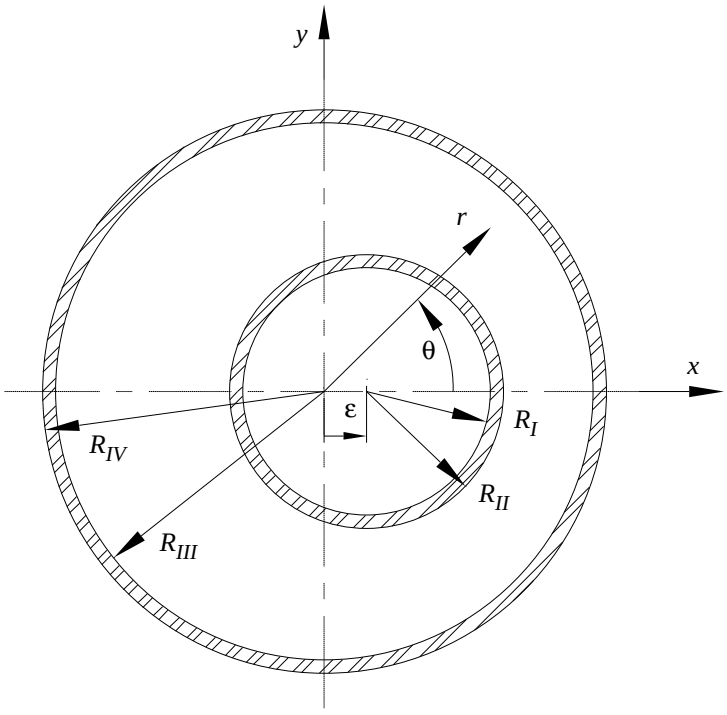

Fig. 9 Misalignment in *x* of the inner conductor: geometry definitions.

As before, we shall assume that the current densities in both inner and outer conductor show no θ-dependence.

In this case, there is no net force. This can be understood if one thinks of the magnetic field as the superposition of two contributions (the problem is linear). Each contribution — a magnetic vector field in its own right — is the result of a specific excitation. The first field is the one resulting from the inner conductor carrying its nominal current, whereby the outer conductor is omitted, given that $\mu_r = 1$ everywhere. The second field results from the outer conductor carrying its nominal current, whereby the inner conductor is omitted. This second field is zero everywhere inside the outer conductor's confinement *($r < R_{III}$)*. Consequently, an observer who undergoes the misalignment displacement ε together with the inner conductor, will not see any change in the field, as long as he observes only this region inside the outer conductor, see Fig. 10. There exists a field distortion in and beyond the outer conductor.

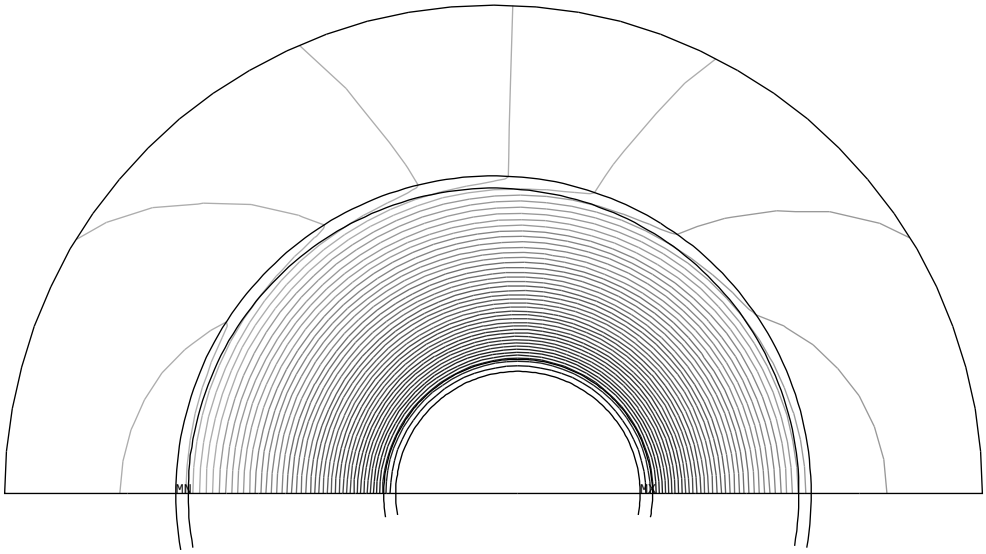

Fig. 10 Flux lines for a misaligned configuration with arbitrary dimensions, from a finite element test run (lower half not shown for symmetry reasons). The tubes and the model's boundary are also drawn. Only a small portion of 'outer space' seems to have been modelled. In fact, additional elements, mapping towards the infinite boundary, have been deployed.

As the field in the inner conductor has not been disturbed by the misalignment, the force system remains unaltered. There is a uniform magnetic pressure. Consequently, there cannot be a net force on the inner conductor. The reaction force on the outer conductor should also vanish, in spite of a force system rearrangement there. This topic will be developed in Appendix A3.

The theory should hold even for larger misalignments, as it is not based on some lower order approximation. However, azimuthal current-density variations may drastically alter the picture. Such rearrangements can result from 'high-frequency' proximity effects (eddy currents) in a misaligned configuration.

Thickness variation of inner conductor; lowest spatial frequency

We will take the following model (see Fig. 11) for a smoothly varying tube thickness:

$$R_{\mathrm{in}} = R_I \qquad R_{\mathrm{out}}(\theta) = R_{II} + \varepsilon \cdot \cos\theta$$

Once more, current densities are assumed to be independent of θ.

Figure 12 depicts the resulting field.

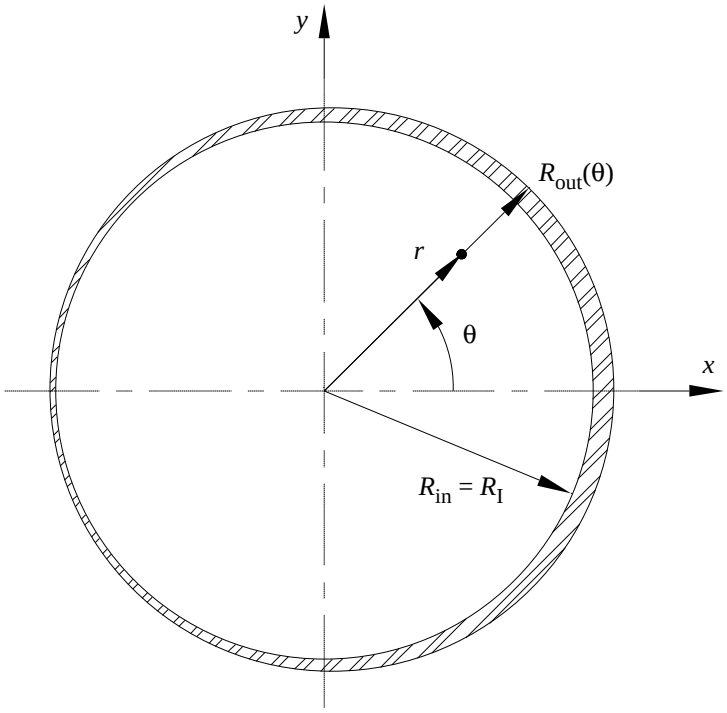

Fig. 11 Thickness variation of inner conductor: geometry definitions.

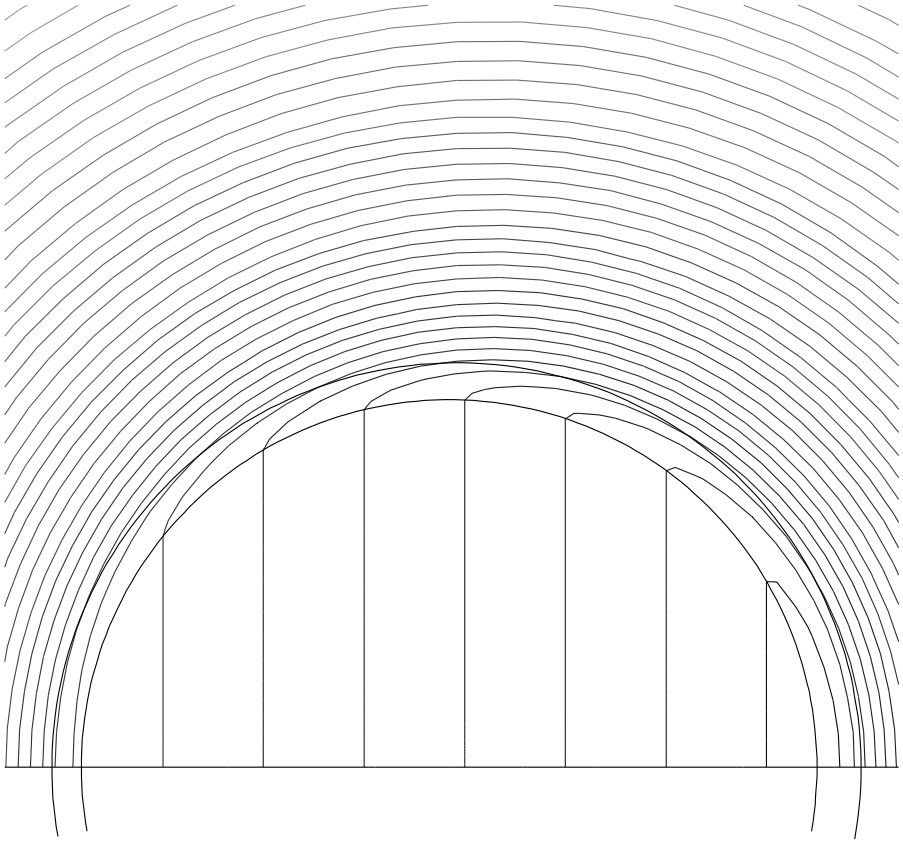

Fig. 12 Flux lines in the vicinity of an inner conductor with thickness perturbation of the cos θ type.

For small ε, a first-order approximate solution to the problem can be found by analytical means, see Appendix A4. The resulting elastic tube deformations have been computed with finite elements, see also Appendix A4. To summarize the results:

- The normal, radial force system is no longer uniform. We shall abandon the term ‘magnetic pressure’, because it becomes rather vague in this new context of geometry imperfections.
- Moreover, a small tangential force density is now developing, of course symmetric with respect to the *x*-axis.
- The total, net force on the tube vanishes again.
- The non-uniform force distribution would inevitably result in bending effects. However, in this specific case, the bending moment turns out to vanish everywhere. The deformation mode thus remains pure compression. Neither deformation responses to increasing load, nor the buckling load, seem to differ from the unperturbed situation.

This behaviour is very special, ideal in some sense. It would therefore be somewhat dangerous to conclude already that thickness imperfections do not make any difference at all.

In the following section another perturbation shape will be tried out.

Thickness variation of inner conductor; higher spatial frequency

We will now investigate a more sensitive thickness variation (see Fig. 13):

$$R_{\text{in}} = R_I \qquad R_{\text{out}}(\theta) = R_{II} + \varepsilon \cdot \cos 2\theta$$

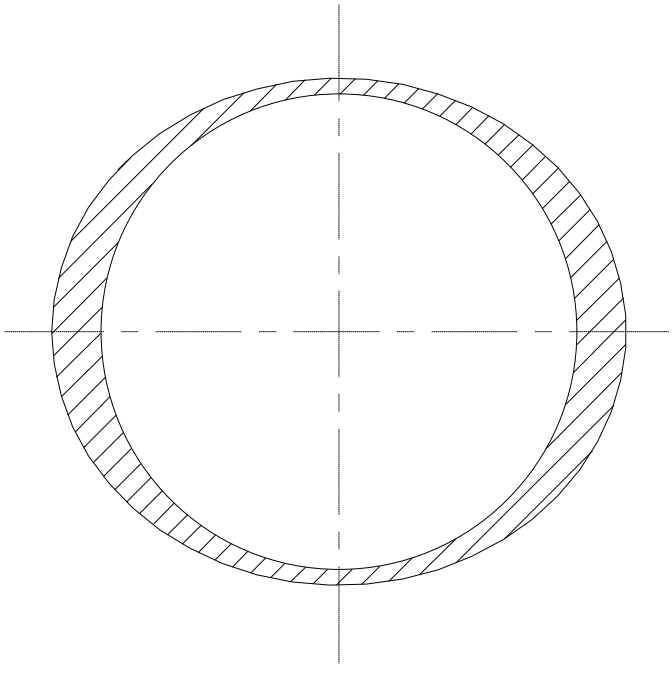

Fig. 13 Thickness perturbation of cos 2θ type.

It has to be admitted that imperfections of this type and of significant amplitude are not very likely to occur in real life. Flux lines are shown in Fig. 14.

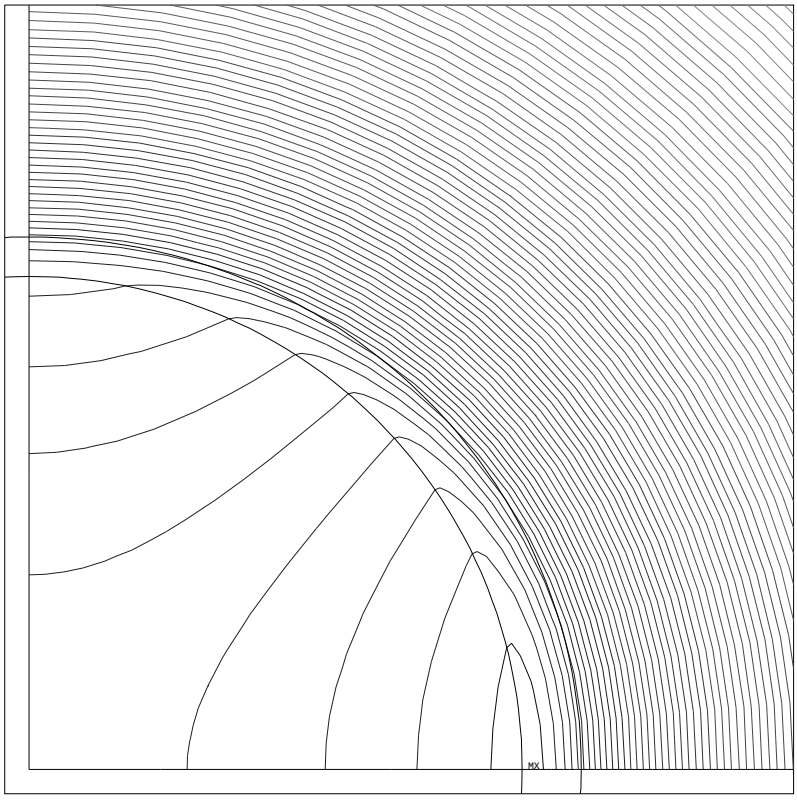

Fig. 14 Flux lines in the vicinity of an inner conductor with thickness perturbation of cos 2θ type. Only the first quarter is depicted, for symmetry reasons.

Detailed discussion is again deferred to Appendix A4; below is a summary.

- The non-uniform force distribution now does result in bending effects. It turns out that the tube is flattened, in the sense that it contracts in *x* and widens in *y*, much like a standing egg.
- This effect is important for tube portions relatively thin with respect to their aperture, such as the entrance portions of our horn.
- There is a relatively small adverse effect on stability (buckling) issues.

Unroundness of inner conductor

Assumed form – see also Fig. 15:

$$R_{\text{in}}(\theta) = R_I + \varepsilon \cdot \cos 2\theta \qquad R_{\text{out}}(\theta) = R_{II} + \varepsilon \cdot \cos 2\theta$$

Flux lines are shown in Fig. 16. The perturbation seems to yield a small effect only.

An in-depth account is given in Appendix A5. The effect is indeed small! Moreover, the developed force distribution tends to ‘beat out’ the imperfection. Unroundness is not believed to cause major problems.

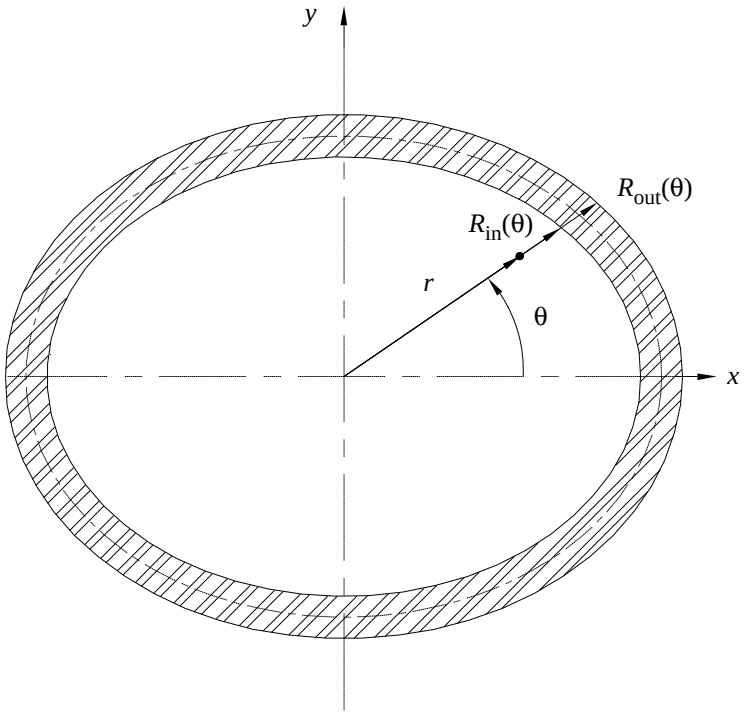

Fig. 15 Unroundness of inner conductor: geometry definitions.

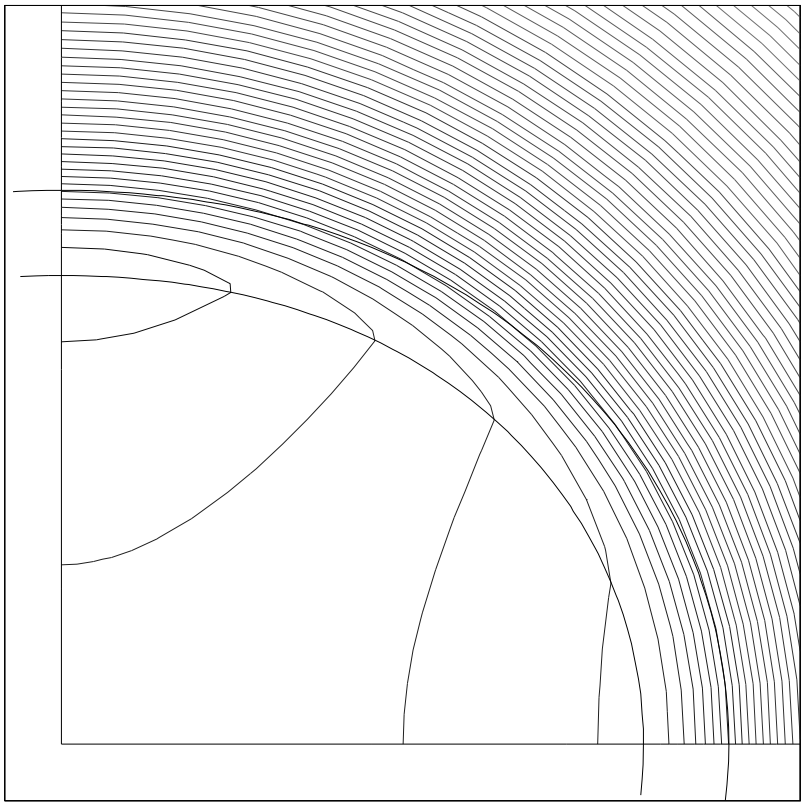

Fig. 16 Flux lines in the vicinity of an inner conductor with exaggerated unroundness.

3 NUMERICAL DEVELOPMENTS

As mentioned before, relatively thick portions become troublesome to solve analytically. If furthermore the transition to the end-caps, see Fig. 2, is to be taken into account, a fully numerical treatment will be inevitable.

In this case, only perfectly axisymmetric geometry is considered.

The way from current injection to mechanical deformations and stresses is paved with three finite element tasks. These tasks are summarized in Table 2, and discussed in the sections below. Interface programs passing data from one task to the next have also been developed..

Table 2
Overview of the three finite element tasks

Task number	1	2	3
Goal	obtain current density pattern $\vec{J}$	obtain flux density pattern $\vec{B}$	obtain deflections/strains/ stresses
Problem type	Poisson (conduction)	magnetostatic/ vector potential $\vec{A}$	structural
Dimensionality	2D axisymmetric	3D ‘slice’	2D axisymmetric
Region modelled	tube portions 9 & 10 exit end-cap up to R = 100 mm	see task 1 slice: 5°	entire horn incl. both end-caps
Body loading	none	$\vec{J}$	$\vec{J} \times \vec{B}$ from tasks 1 & 2 in the region covered by these tasks; surface loading elsewhere
Other loading	none	none	surface loading from analytical recipes on end-caps; 1010 N from Fig. 7 as nodal forces
Boundary conditions/ boundary loading	100 kA injection on one side; homogeneous Dirichlet on other	see Fig. 18	simple axial support at flanges
Treated in section	3.1	3.1	3.2

The Ansys[1] finite element code has been used

The figures below, often zoom plots, correspond to a horizontal beam axis, pointing to the right. They represent longitudinal sections, like Fig. 2. The finite element grid itself is mostly not shown. The beam axis is depicted whenever possible.

The Ansys input files for each task (`horn1.inp, horn2.inp, horn3.inp`), as well as the the source codes (Fortran90) for the interface programs (`horn12.f, horn23.f`) are available at

`/afs/cern.ch/user/w/wertelae/public/horn`

3.1 Electromagnetic finite element model of the exit region

The following contains a discussion on finite element (FE) modelling of the last two portions, 9 and 10 (9 starting at z = 6275 mm), together with a piece of end-cap sheet (up to radius 100 mm).

The first FE task solves the Laplace equation, on a 2D axisymmetric problem, in order to obtain the current density field resulting from a 100 kA injection.

The result in the transition region is plotted in Fig. 17. The peak value remains limited to some 250 A/mm^2, less than the 280 obtained at the entrance of portion 9. Thanks to the generous rounding radius: the current can ‘take the curve’ relatively easily.

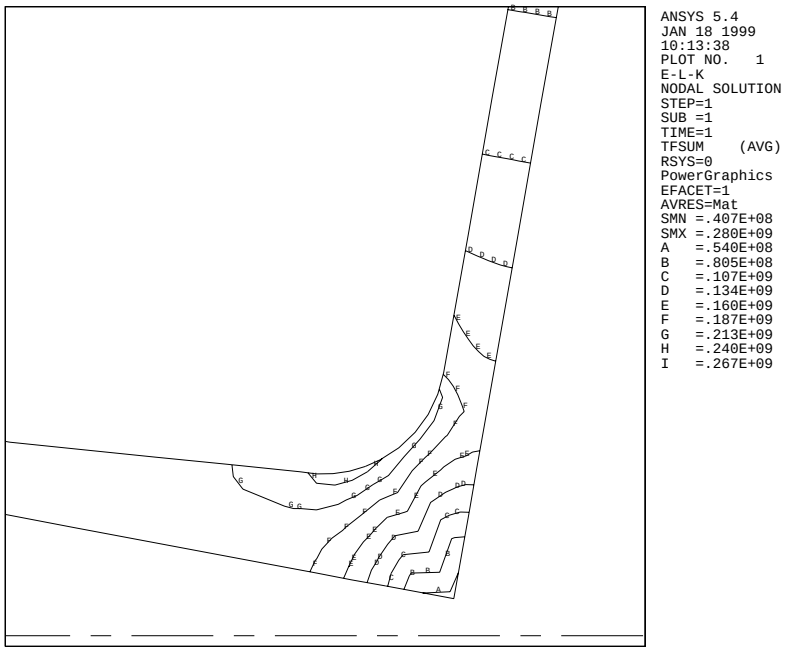

Fig. 17 Isolines of current density vector magnitudes, in A/m^2; result of the ‘first task’. Unrealistic kinks in the corner region are due to finite element approximation problems, amplified by a distorted grid. The SMN and SMX entries in the legend column are the minimum and maximum values, respectively.

1. Ansys® is a registered trademark of Swanson Analysis Systems Inc., Houston (PA), USA

With the current-density results we shall now, in the second task, find the flux densities. Only the B_θ component is non-zero.

Unfortunately this is not a classical 2D axisymmetric magnetic finite element problem:

With vector potential $\vec{A}$ satisfying $\vec{B} = \overrightarrow{curl}\ \vec{A}$, we have for a classical problem a solenoidal current:

$$\vec{J} = (0, J_\theta, 0) \qquad \vec{A} = (0, A_\theta, 0) \qquad \vec{B} = (B_r, 0, B_z) \ .$$

The horn problem is in a way just the opposite, a toroidal field:

$$\vec{J} = (J_r, 0, J_z) \qquad \vec{A} = (A_r, 0, A_z) \qquad \vec{B} = (0, B_\theta, 0) \ .$$

Neither can the problem at hand be translated, via some analogy, to a Poisson-like problem, because our governing equation is

$$\overrightarrow{curl}\left(\frac{1}{\mu} \cdot \overrightarrow{curl}\ \vec{A}\right) = \vec{J} \ ,$$

giving rise to a few inevitable minus signs, also in cylindrical coordinates, which is definitely not the case for a Poisson-type problem:

$$div\ (\lambda \cdot \overrightarrow{grad}\ T) = -q''' \ .$$

The following strategy has been deployed.

The node pattern of our first FE task (half-plane $\theta = 0$) is to be copied to $\theta = -\Delta\theta/2$ and to $\theta = +\Delta\theta/2$. A 3D model, as rational as possible, is then constructed between these two new half-planes, i.e. only one brick element layer. The element connectivity (its nodes) of the 2D model is used to generate this one layer of brick elements. This is one of the tasks performed by the interface program.

Quite some air has to be modelled around the horn's flesh. Indeed, this modelling work has also been prepared in the first task's preprocessing

We end up with a slender 'piece of cake', see Fig. 18, with opening angle $\Delta\theta$, chosen to be 5°. Needless to say, the 2D model (half-plane $\theta = 0$) is deactivated during the 3D magnetostatic solution.

The magnetic vector potential formulation $(\vec{A})$ is used.

The reason why only part of the conductor and end-cap have been considered may now become clear. Owing to the apparent need to include much of the surrounding air, a full model would become very big.

Another responsibility of the interface program is to retrieve the current-density solution from the first task and to apply these currents as body loading to the second task.

By far the most difficult problem has been to find suitable boundary conditions for the magnetic potential. Our exercise is very untypical, and in spite of great effort, the applied boundary conditions are believed to be, rigorously, not entirely correct. But they are thought to be quite adequate for our purposes. A few checks can be made on the flux density results, see Fig. 19.

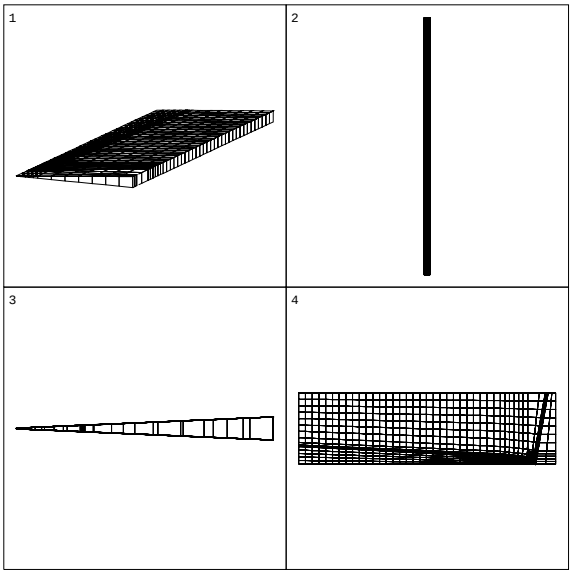

Fig. 18 Finite element model for the ‘second task’, seen from various viewpoints. For the horn itself, there are eight element layers ‘through-thickness’. The total model contains 995 3D elements, mostly bricks, plus a few wedges. Applied boundary conditions: $A_r = 0$ at inner radius and at z end-planes; $A_\theta = 0$ at θ end-planes; $A_z = 0$ at outer radius.

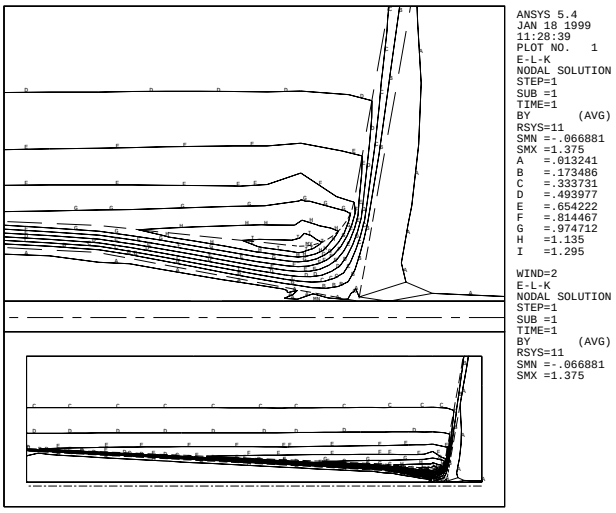

Fig. 19 Isolines of constant flux density B_θ (in tesla) result of the ‘second task’. Top: zoom into transition region. Bottom: entire model. A small signal is observed where it is not expected (line ‘A’), owing to postprocessor interpolation/averaging and to ‘imperfect’ boundary conditions. Outside the tube, isolines should be parallel to the beam axis. This ideal pattern is somewhat disturbed (e.g. line ‘F’). The reason is believed to be a locally rather coarse and distorted element grid. The unlabelled solid lines are the FE model’s boundaries.

A second interface program takes the current densities from the first task and the flux densities from the second task, performs the Lorentz outer product, and applies the result as mechanical body loading to the third FE task. This mechanical problem is again 2D axisymmetric. The 3D model can be deleted, as well as the 2D ‘air’ nodes and elements. The 2D horn elements from the first task are reactivated and converted to a mechanical type.

It should be noted that such a mechanical model would be largely incomplete. Only a small fraction of the exit end-cap is present, moreover the entrance end-cap is completely absent. Analysis of this preliminary model revealed that axial deformations are the main source of stress development. An extension to this model was judged necessary. The final mechanical model — reported upon below — contains both end-caps and the entire tube.

3.2 Mechanical finite-element model of the entire horn

The electromagnetic loading of portions 1–8 of the tube has been simplified to a global, axial force of 1010 N, pulling upstream. The magnetic pressure on the exit end-cap — for radii above 100 mm — as well as for the entire entrance end-cap, has been determined by analytical approximations, and input as FE surface loads.

Boundary conditions for this (revised) third task are simple axial support at the rim of each of the end-caps. The model is in some way overconstrained. We implicitly assume stress-free mounting and no thermal expansion trouble.

The resulting deformations are shown in Fig. 20.

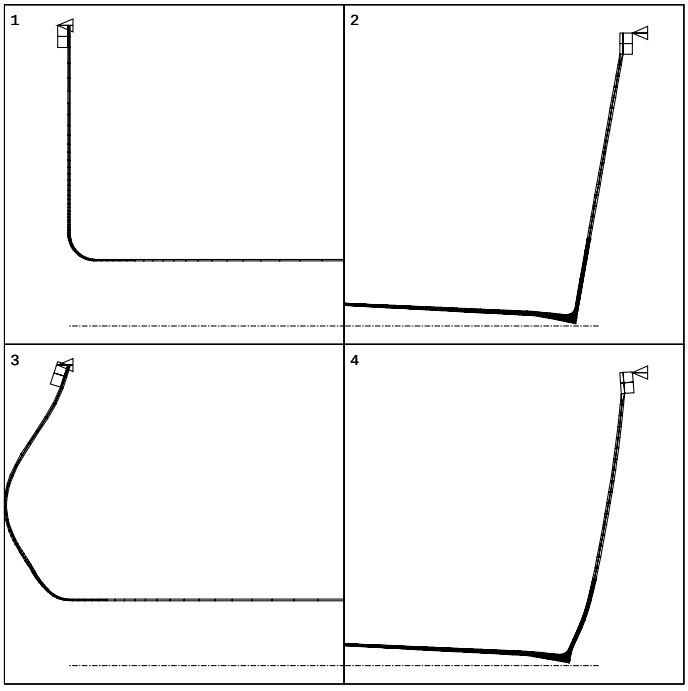

Fig. 20 Deformations of the horn’s entrance and exit regions: result of the ‘third task’. Top: undeformed. Bottom: deformed, exaggeration factor of 200 applied to deflections. The triangles indicate the boundary conditions: simple axial support. Maximum deflection: about 0.38 mm.

Electromagnetic force inventory, axial components.

- Entrance end-cap: 1430 N, upstream (analytical).
- Portions 1–8: 1010 N, upstream (analytical).
- Portions 9 and 10, upstream contribution: 937 N (FE result)
- Portions 9 and 10, downstream contribution, and exit end-cap part up to diameter 200 mm: 2153 N (FE result).
- Remainder of exit end-cap: 1163 N, downstream (analytical).

This yields a total upstream force of 3377 N, and a total downstream force of 3316 N. To within 61 N, or some 2%, they are of equal magnitude.

After solving the mechanical problem, the following reaction forces are found.

- Entrance end-cap's flange: 519 N, trying to push the horn downstream.
- Exit end-cap's flange: 458 N, trying to push the horn upstream.

Evidently, the same 61 N discrepancy is found.

These reaction forces are axial, corresponding to the modelled boundary conditions.

Stresses are plotted in Figs. 21–26: They are of moderate magnitude. The reasons are not only:

- thick-walled tube near exit,

but perhaps even more important:

- stiff exit end-cap: thick and slightly conical;
- generous rounding radii from tube to end-caps.

One should consider applying a microball bombardment to the highly stressed surface regions in order to make them more fatigue-resistant.

The following result figures each contain four zoom plots: entrance region (left); exit region (right); outer flange region (top); tube region (bottom). Meaningful signals obtained in regions not captured by these zoom plots are quoted in the appropriate figure captions. The letter codes refer to the legend column at the right hand side of each plot.

We are facing a potential fatigue problem. It is normal practice to confront the obtained stresses with fatigue data, such as Wöhler curves, available for that specific material. The problem is that such data are normally obtained from uniaxial testing, mostly tension or tension/compression. In real-life devices one mostly has a multiaxial stress state. This problem is similar to that of estimating yielding risks, i.e. the onset of plastic deformation. The classical recipe is to work out an 'equivalent stress': The multiaxial stress state is condensed down to one stress, and this for every point in space. This equivalent stress is to replace the actual stress state in assessing some limit criterion. A limit criterion can be

- yielding onset;
- brittle rupture;
- fatigue.

A well-known example is that of the von Mises equivalent stress σ_{VM} combined with a yielding onset limit criterion. It is computed as follows:

$$2\sigma_{\mathrm{VM}}^2 = (\sigma_I - \sigma_{II})^2 + (\sigma_{II} - \sigma_{III})^2 + (\sigma_{III} - \sigma_I)^2$$

where σ_I, σ_{II} and σ_{III} are the principal stresses. We can also write, in our specific case where two shear stresses vanish,

$$\sigma_{\mathrm{VM}}^2 = \sigma_r^2 + \sigma_\theta^2 + \sigma_z^2 - (\sigma_r\sigma_\theta + \sigma_\theta\sigma_z + \sigma_z\sigma_r) + 3\tau_{rz}^2 \ .$$

The von Mises hypothesis states that its accompanying equivalent stress is equally as bad as the stress state it replaces. In the context of yielding onset, plastic deformation would commence whenever or wherever the von Mises stress were greater than the uniaxial yield strength. Such a hypothesis is not more than a theory. There exist several other hypotheses, such as Lamé and Tresca. The Tresca and von Mises hypotheses have demonstrated acceptable results when the limit criterion is yielding onset and the material is a ductile metal. The von Mises stress is the more popular one, mainly because of its straightforward computational recipe.

Now, according to Ref. [5], the Tresca and von Mises stresses can also be used, given ductile materials, when the limit criterion is fatigue failure. So we propose tentatively to confront the results of Fig. 26 with the available fatigue data.

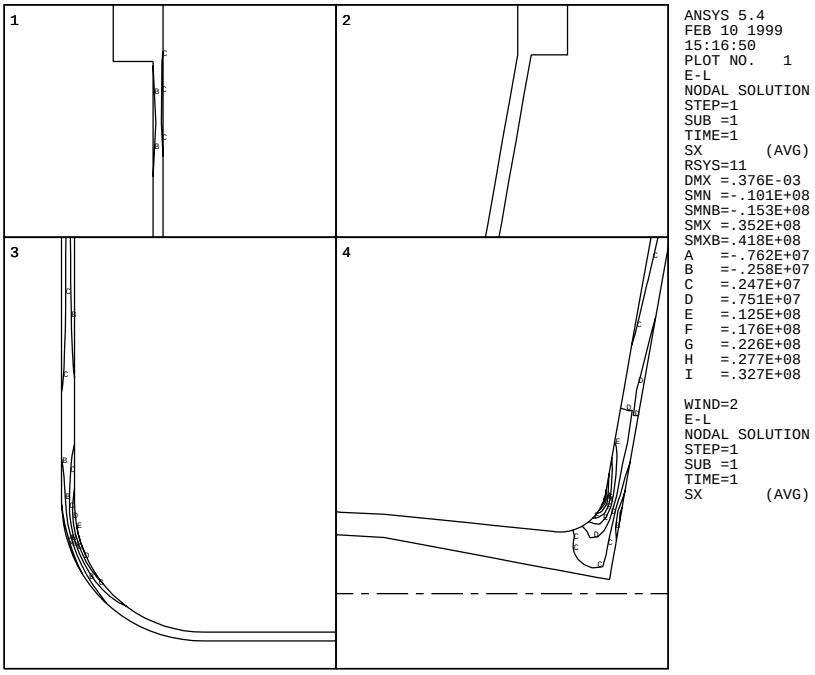

Fig. 21 Normal stress σ_r (radial) in Pa, positive for tensile and negative for compressive — the usual convention for normal stresses. The diaphragm bending of the end-cap sheet gives a clear concentration effect near the transition. Stress levels in the end-cap sheet, ‘half-way’ between tube and flange (radii 100–200 mm): C to A (from left to right, through thickness) for entrance, about C for exit.

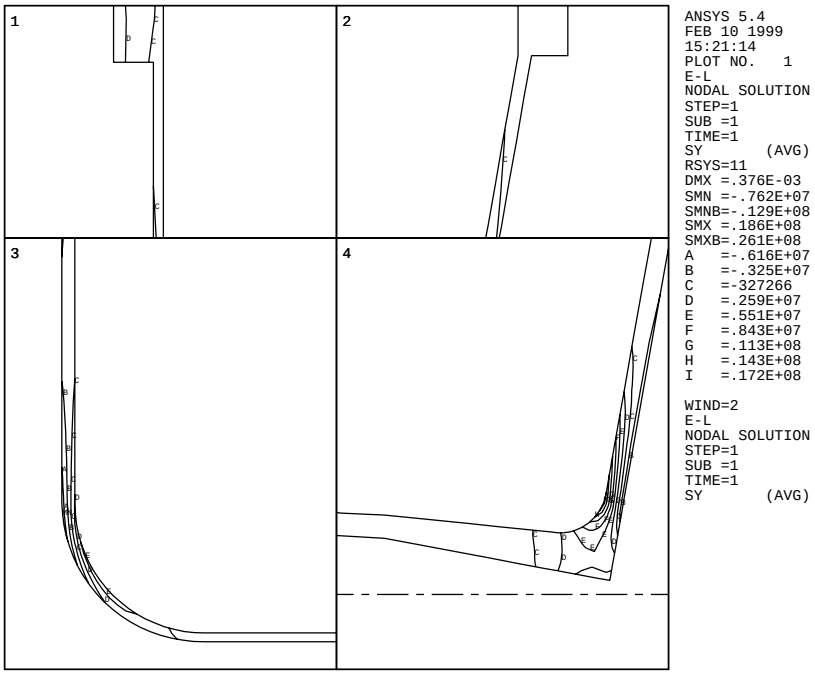

Fig. 22 Normal stress σ_θ (hoop) in Pa. Horn's tube compression is hardly visible thanks to adequate thickness. End-cap bending is nicely visible. Stresses in the end-cap sheet, 'half-way': C to B for entrance, between B and C for exit.

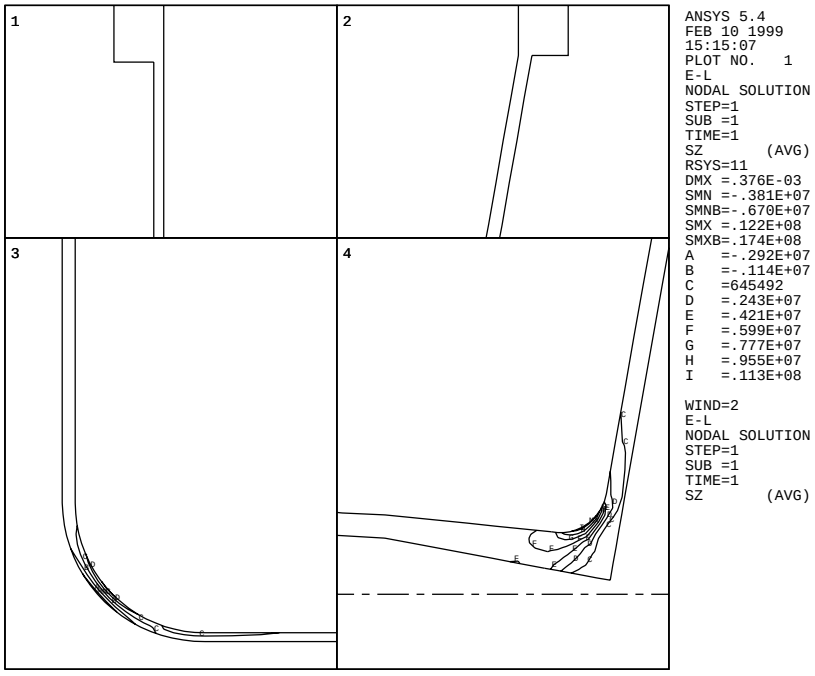

Fig. 23 Normal stress σ_z (axial) in Pa: typically some 1 to 6 MPa of traction in the tube (not visible on these zoom plots). Bending stress concentration is again nicely visible. Stresses in the end-cap sheet, 'half-way': about C both for entrance and exit.

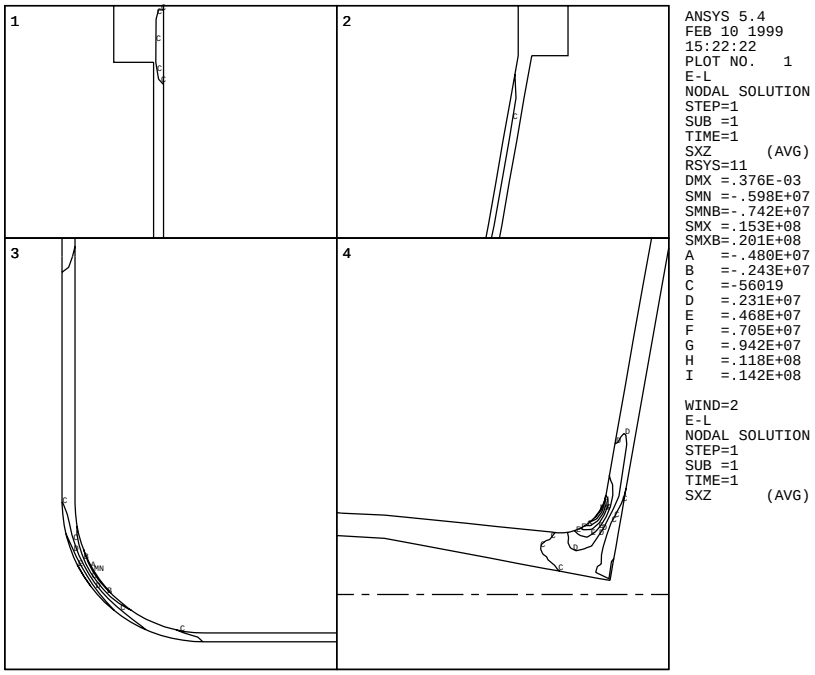

Fig. 24 Shear stress τ_{rz} in Pa. Apart from the ever-present bending effect, there is nothing significant to report. The remaining shear stresses, $\tau_{r\theta}$ and $\tau_{\theta z}$, are zero thanks to axisymmetry. Stresses in the end-cap sheet, 'half-way': about C for both entrance and exit.

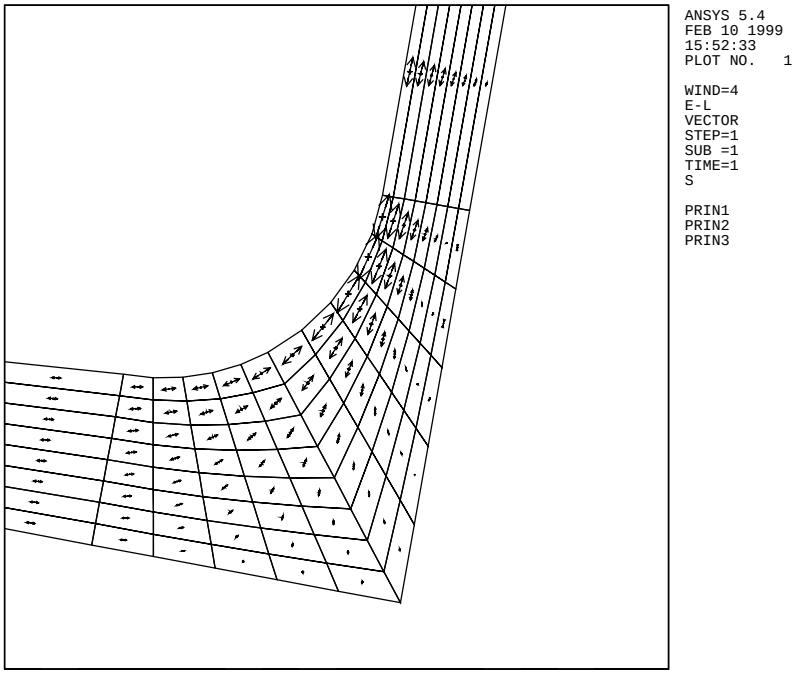

Fig. 25 The stress state represented under the form of the orthogonal system of three principal stresses, two of which are in-plane thanks to axisymmetry.

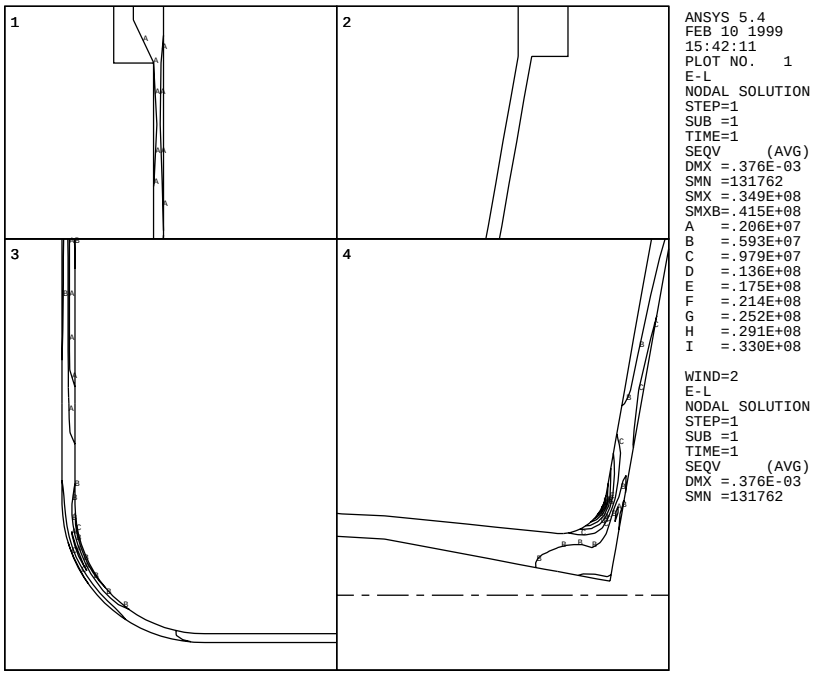

Fig. 26 Von Mises equivalent stress σ_{VM} in Pa.

4 CONCLUSIONS AND OUTLOOK

- It is important that one end-cap be axially very stiff, and the other sufficiently compliant. This avoids problems with tolerances and with differences in thermal expansion. The inner conductor may be assumed to get hotter than the outer one. There is no doubt that the exit end-cap has to be the stiffer one.
- The inner conductor portions of large diameter — and small thickness — seem to suffer neither from too high a compressive stress level, nor from elevated buckling risks, not even in the case of a considerable working current increase.
- The horn does not appear to be exposed to much extra risk due to cross-sectional geometry imperfections. We have proven that a transverse misalignment does not, under normal circumstances, induce a net force. Small thickness variations of lowest spatial frequency, if approximated with a cos θ law, give a force system such that bending effects cancel out, and the tube simply remains loaded in a purely compressive mode. Modelled thickness variations of higher spatial frequency do yield important bending signals; however the likelihood of such imperfections occurring is questionable. Unroundness-type imperfections give only small mechanical perturbations; moreover they are of stabilizing nature.
- The axial effects are the main source of concern. The Lorentz forces in the end-caps are of mainly axial signature. Diaphragm bending of the end-caps is the result. Moreover, the tube itself is slightly conical, so the magnetic pressure has a net axial component. The coupling into the tube gives rise to stress concentrations. The exit end-cap needs to be stiff. Not a conical aspect alone, or a thick sheet alone, but a combination of both, seems

the most attractive way to proceed. A big rounding radius at the tube/end-cap transition is vital.

- The end-cap flanges are a bit meagre.
- Four-point current injection into the outer flange of one of the end-caps is not believed to give noticeable perturbations in the tube's current-density pattern.
- The dynamic aspects have not been considered. It shall however be kept in mind: every attempt to smooth the current pulse waveform at its 'roots' pays off in the form of a drastic reduction in harmonics content, with only modest penalty to the Joule dissipation budget.

Acknowledgements

The computational work reported here, has been the result of a request from J.-M. Maugain and S. Rangod to the CERN/EP/TA-2 group.

References

[1] M. Giesch et al., Nucl. Instrum. Methods, 20 (1963) 58.

[2] Y. Yamanoi et al., Large horn magnets at the KEK neutrino beam line, Proc. 15th Int. Conf. on Magnet Technology (MT15), Beijing, 1997, KEK Preprint 97–225.

[3] G. Acquistapace et al., The CERN neutrino beam to Gran Sasso (NGS): Conceptual technical design, CERN 98–02, INFN/AE–98/05, Geneva (1998).

[4] J.M.T. Thompson and G.W. Hunt, A general theory of elastic stability, Wiley, London (1973).

[5] Dubbel - Taschenbuch für den Maschinenbau, 17. Auflage, Springer, Berlin, (1990), page E5.

APPENDIX A1

AZIMUTHAL NON-UNIFORMITIES OF THE CURRENT DENSITY DUE TO 4-POINT INJECTION

Instead of being uniformly distributed over the full flange circumference, the current would in practice be fed at four ‘concentrated stations’. So the current system would exhibit a θ-dependence, albeit with a 90-degree periodicity.

The problem can be studied in an elegant way with a two-dimensional axisymmetric FE model, Fig. 27. The loading would be decomposed into its circular Fourier components. A FE solution for each of the harmonics would now be found. Linearity of the problem imposes that the result show the same spatial frequency (therefore: order number) as the loading. The responses to all the harmonics would then be superimposed in the postprocessor. It is again the problem’s linearity that allows such superposition.

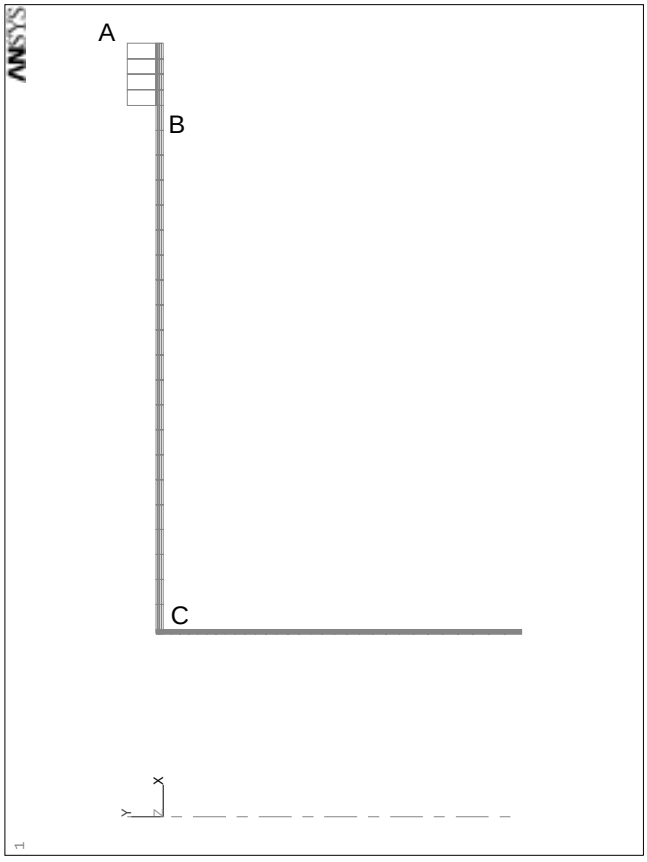

Fig. 27 Two-dimensional, axisymmetric finite element model of a simplified entrance end-cap region. The current is assumed to be fed at the flange, ‘point A’. Flange dimensions: inner radius 298 mm, outer radius 324 mm, thickness 15 mm, corresponding to a design which is now superseded. ‘Point B’ on the end-cap (3 mm thick and ‘point C’ (at the start of the horn, see Table 1) are measurement stations. These ‘points’ are in fact 90-degree circular arcs perpendicular to the beam axis, arcs along which the θ-dependence will be examined. The reader is invited to ignore the Ansys coordinate system.

A function reasonably approximating the localized current injection, could look like this:

$$f(\theta) = \left(\cos\frac{\pi\theta}{2L}\right)^2 \quad \text{for } -L \le \theta \le L \ , \quad \text{and}$$

$$f(\theta) = 0 \quad \text{elsewhere,} \qquad L = \pi/16 = 11.25° \ .$$

The following truncated Fourier series is taken as an approximation to $f(\theta)$ to be used for the model's loading:

$$f_{\text{approx}}(\theta) = a_0 + \sum_{k=1}^{7} a_k \cos 4k\theta$$

where

$$a_0 = \frac{1}{8}$$

$$k \ge 1 \ : \qquad a_k = a_{k1} + a_{k2}$$

$$\pi \cdot a_{k1} = \frac{1}{8+2k} \cdot \sin\left[\left(1+\frac{k}{4}\right)\cdot\pi\right] - \frac{1}{8-2k} \cdot \sin\left[\left(1-\frac{k}{4}\right)\cdot\pi\right] \qquad a_{4,1} = \frac{1}{8}$$

$$a_{k2} = \frac{1}{\pi k} \cdot \sin\left(\frac{\pi k}{4}\right) \ .$$

This function would have to be properly scaled to get the total current right.

Figure 28 depicts the resulting loading profile.

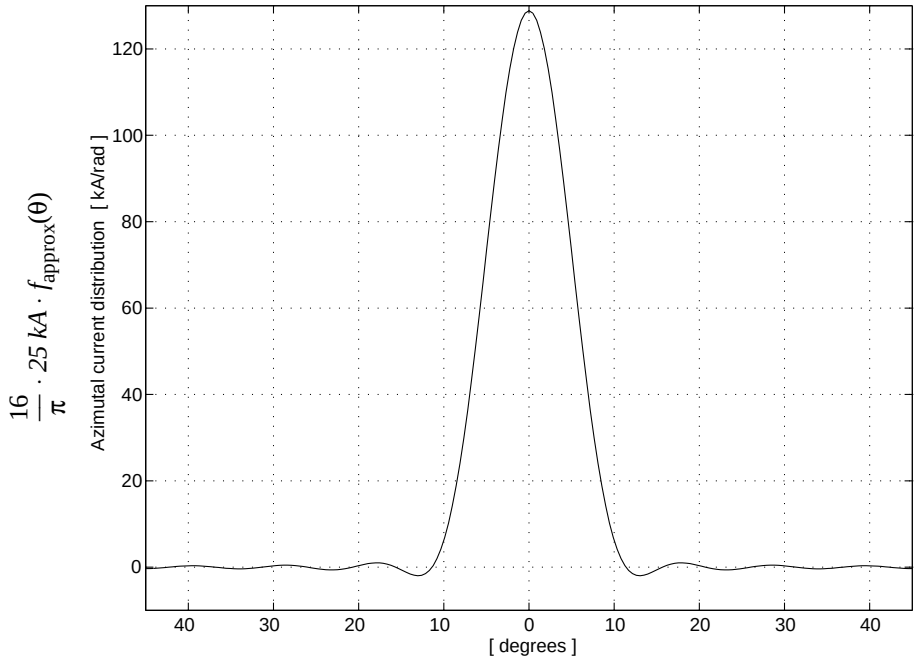

Fig. 28 Modelled current distribution, injected at station A, as a function of θ. The total current for the represented 90-degree arc indeed amounts to 25 kA (curve integration with θ expressed in radians).

The disturbance dies out very quickly: Figs. 29 and 30 give an impression.

The conclusion is that once well into the horn's tube part, the azimuthal variation of current density is really negligible.

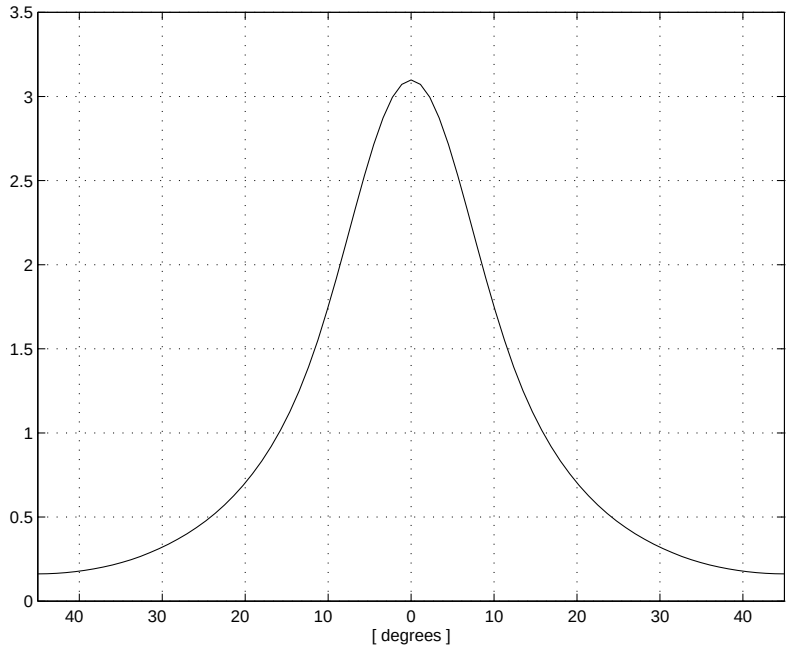

Fig. 29 Resulting current density (magnitude of vector), 'measured' at station B, as a function of θ. Normalized to its average value, being 18.3 A/mm^2.

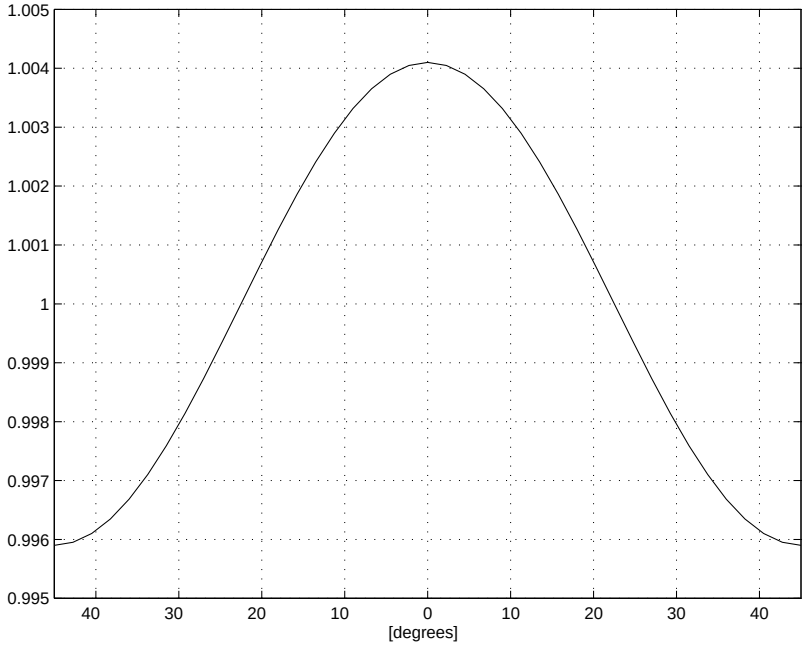

Fig. 30 Resulting current density (magnitude of vector), 'measured' at station C, as a function of θ. Normalized to its average value, being 110 A/mm^2. Remark: the θ-dependence decreases very rapidly as the measurement location is moved downstream.

APPENDIX A2

MAGNETIC POTENTIAL AND FLUX DENSITIES FOR SIMPLE GEOMETRIES

In the following we will make intensive use of the magnetic vector potential

$$\vec{A} = (A_r, A_\theta, A_z)$$

satisfying

$$\vec{B} = \overrightarrow{curl}\ \vec{A} \ ,$$

which implicitly imposes $div\ \vec{B} = 0$.

The field is two-dimensional ($B_z = 0$). It follows then, from the nature of the curl operator, that

$$A_r = 0 \ , \qquad A_\theta = 0 \ ;$$

and hereafter A_z will be denoted by A, keeping in mind that it bears a sign.

For a 2D problem, equipotential lines are flux lines.

We will try to solve the problem for A, and derive from it the flux density components:

$$B_r(r, \theta) = \frac{1}{r} \cdot \frac{\partial A}{\partial \theta} \ , \qquad B_\theta(r, \theta) = - \frac{\partial A}{\partial r} \ .$$

The differential form of Ampère's law,

$$\overrightarrow{curl}\ \vec{H} = \vec{J} \ ,$$

condenses down to a scalar equation. In the absence of permeable materials,

$$\frac{\partial B_\theta}{\partial r} - \frac{1}{r} \cdot \frac{\partial B_r}{\partial \theta} + \frac{B_\theta}{r} = \mu_0 \, J(r, \theta) \ .$$

The above equations specialize further in the case of a perfect cylindrical problem:

$$B_r = 0 \ , \qquad B_\theta(r) = - \frac{\mathrm{d}A}{\mathrm{d}r}$$

$$\frac{\mathrm{d}B_\theta}{\mathrm{d}r} + \frac{B_\theta}{r} = - \frac{\mathrm{d}^2 A}{\mathrm{d}r^2} - \frac{1}{r} \cdot \frac{\mathrm{d}A}{\mathrm{d}r} = \mu_0 \, J(r) \ .$$

Solution in the special case of constant J:

$$A(r) = - \frac{\mu_0 J r^2}{4} - const \cdot \ln \frac{r}{R_{\mathrm{ref}}} + const \ ,$$

in which R_{ref} would be a constant, conveniently chosen, bearing the dimension of a length.

More specifically, for each of the different regions surrounding the inner conductor:

$$R_{II} \le r : \qquad A = -c_0 \cdot \ln\frac{r}{R_{II}} + d_0 \qquad \text{(no currents)} \ .$$

$$R_I \le r \le R_{II} : \qquad A = -\frac{\mu_0 J r^2}{4} - c'_0 \ln\frac{r}{R_{II}} + d'_0 \ .$$

$$0 \le r \le R_I : \qquad A = d''_0 \ \text{(no currents ; logarithmic term would diverge)} \ .$$

The interface conditions to be imposed are the continuity of both A and $\mathrm{d}A/\mathrm{d}r$ at $r = R_I$ and $r = R_{II}$, yielding four conditions for five integration constants. In order to avoid floating potential, we need to clamp A, say to zero value, at some location, say $r = 0$. After working out,

$$c_0 = \frac{\mu_0 J}{2} \cdot (R_{II}^2 - R_I^2) \ , \qquad d_0 = \frac{\mu_0 J}{4} \cdot \left[R_I^2 \cdot \left(1 - 2\ln\frac{R_I}{R_{II}}\right) - R_{II}^2 \right] \ ,$$

$$c'_0 = -\frac{\mu_0 J}{2} \cdot R_I^2 \ , \qquad d'_0 = \frac{\mu_0 J}{4} \cdot R_I^2 \cdot \left(1 - 2\ln\frac{R_I}{R_{II}}\right) \ ,$$

$$d''_0 = 0 \ .$$

These developments serve as preparation for Appendices A3, A4 and A5.

Remark

Suppose we had following potential, to describe some small imperfection:

$$A(r, \theta) = \alpha_0(r) + \alpha_k(r) \cdot \cos k\theta \qquad k \ge 1$$

in which α_k represents the amplitude, itself a function of r, of a disturbance wave of circular order k. Nature's beauty imposes that α_0 correspond to the perfectly axisymmetric potential.

The flux density components:

$$B_r(r, \theta) = -k\,\frac{\alpha_k}{r} \cdot \sin k\theta \ , \qquad B_\theta(r, \theta) = -\frac{\mathrm{d}\alpha_0}{\mathrm{d}r} - \frac{\mathrm{d}\alpha_k}{\mathrm{d}r} \cdot \cos k\theta \ .$$

Ampère's law:

$$-\frac{\mathrm{d}^2\alpha_0}{\mathrm{d}r^2} - \frac{\mathrm{d}^2\alpha_k}{\mathrm{d}r^2} \cdot \cos k\theta + k^2\,\frac{\alpha_k}{r^2} \cdot \cos k\theta - \frac{1}{r} \cdot \frac{\mathrm{d}\alpha_0}{\mathrm{d}r} - \frac{1}{r} \cdot \frac{\mathrm{d}\alpha_k}{\mathrm{d}r} \cdot \cos k\theta = \mu_0 \cdot J(r, \theta)$$

would in fact yield two equations: one for the 'DC component', and one for the cos $k\theta$ wave. In the case of constant current density,

$$-\frac{\mathrm{d}^2\alpha_0}{\mathrm{d}r^2} - \frac{1}{r} \cdot \frac{\mathrm{d}\alpha_0}{\mathrm{d}r} = \mu_0 J \qquad \text{yielding} \qquad \alpha_0(r) = -\frac{\mu_0 J r^2}{4} - c_0 \cdot \ln\frac{r}{R_{\mathrm{ref}}} + d_0 \ ,$$

and

$$\frac{\mathrm{d}^2\alpha_k}{\mathrm{d}r^2} + \frac{1}{r} \cdot \frac{\mathrm{d}\alpha_k}{\mathrm{d}r} - k^2\,\frac{\alpha_k}{r^2} = 0 \qquad \text{yielding} \qquad \alpha_k(r) = c_k r^k + d_k r^{-k} \ ,$$

respectively. (Primes and double primes for the integration constants have been omitted.)

These results will be used in Appendix A4 for k=1 and 2, and in Appendix A5 for k=2.

APPENDIX A3

MISALIGNMENT OF INNER CONDUCTOR

In order to evaluate the force system non-uniformities in the outer conductor, we shall again use the idea of decomposition into two contributions. In the second contribution, only the outer conductor carries current. This results in a uniform pressure on the outer conductor. This second contribution consequently does not need further consideration. In the first contribution, only the inner conductor carries current. It corresponds to the following potential in the vicinity of the outer conductor:

$$A_i = -c_i \cdot \ln \frac{r'}{R_{\text{ref}}} \qquad \text{with} \qquad c_i = \frac{\mu_0 I}{2\pi} \ ,$$

in which r' is the radial position seen from the inner conductor's centre. It is related to r (Fig. 9) via the cosine rule:

$$r'^2 = r^2 + \varepsilon^2 - 2r\varepsilon \cos\theta$$

The relevant derivatives can be obtained with the chain rule:

$$\frac{\partial A_i}{\partial r} = \frac{\partial A_i}{\partial r'} \cdot \frac{\partial}{\partial r} r' = -c_i \cdot \frac{r - \varepsilon \cos\theta}{r^2 + \varepsilon^2 - 2r\varepsilon \cos\theta} \ ,$$

$$\frac{\partial A_i}{\partial \theta} = \frac{\partial A_i}{\partial r'} \cdot \frac{\partial}{\partial \theta} r' = -c_i \cdot \frac{r\varepsilon \sin\theta}{r^2 + \varepsilon^2 - 2r\varepsilon \cos\theta} \ .$$

With force density per unit volume,

$$\vec{f}(r, \theta) = (f_r, f_\theta, 0) = \vec{J} \times \vec{B} \ ,$$

we obtain, in the outer conductor with constant current density J_o, the force density due to the 'first contribution':

$$f_r = -J_o \cdot B_\theta = J_o \cdot \frac{\partial A_i}{\partial r} \ , \qquad f_\theta = J_o \cdot B_r = \frac{J_o}{r} \cdot \frac{\partial A_i}{\partial \theta} \ .$$

The total horizontal force on the outer conductor, per unit depth *(z)*, due to the 'first contribution' :

$$p_x = \int_{R_{III}}^{R_{IV}} \int_0^{2\pi} (f_r \cos\theta - f_\theta \sin\theta)\, r \, d\theta \, dr \ .$$

It remains to be shown that p_x vanishes.

Integration through the tube's thickness is not necessary; the expression will vanish 'fibre by fibre'. For reasons of symmetry, azimuthal integration up to π only should suffice.

Now,

$$\frac{1}{J_o c_i} \cdot (f_r \cos\theta - f_\theta \sin\theta) = \frac{\varepsilon - r \cos\theta}{r^2 + \varepsilon^2 - 2r\varepsilon \cos\theta} \ .$$

So we end up with a task of the form

$$\int_0^{\pi} \frac{a + b\cos\theta}{c + \mathrm{d}\cos\theta}\,\mathrm{d}\theta \;=\; 2 \cdot \int_0^{\infty} \frac{a(1+u^2) + b(1-u^2)}{c(1+u^2) + \mathrm{d}(1-u^2)} \cdot \frac{1}{1+u^2}\mathrm{d}u$$

$$= \frac{2}{c-\mathrm{d}} \cdot \left[\int_0^{\infty} \frac{\alpha}{u^2+k^2}\mathrm{d}u + \int_0^{\infty} \frac{\beta}{u^2+1}\mathrm{d}u \right]$$

$$= \frac{2}{c-\mathrm{d}} \cdot \left[\frac{\alpha}{k} \cdot \lim_{v\to\infty} \operatorname{atan}\frac{u}{k}\Big|_0^{v} + \beta \cdot \lim_{v\to\infty} \operatorname{atan} u\Big|_0^{v} \right] \;=\; \frac{2}{c-\mathrm{d}} \cdot \frac{\pi}{2} \cdot \left(\frac{\alpha}{k} + \beta\right)$$

with the substitutions

$$a = \varepsilon\,, \qquad b = -r\,, \qquad c = r^2 + \varepsilon^2\,, \qquad d = -2r\varepsilon\,, \qquad u = \tan\frac{\theta}{2}\,,$$

$$k = \sqrt{\frac{c+d}{c-d}} = \frac{r-\varepsilon}{r+\varepsilon}\,, \qquad \beta = \frac{2b}{k^2-1}\,, \qquad \alpha = a - b - \beta\,,$$

from which it can be readily shown that $\alpha + \beta k = 0$.

It is important to note the rigorous application of the nonlinear cosine rule, without first-order or other approximations. The proof that the total *x*-force vanishes obviously also holds for larger misalignments.

APPENDIX A4

THICKNESS VARIATION OF INNER CONDUCTOR: FIRST-ORDER PERTURBATIVE ANALYSIS

Lowest spatial frequency

Definitions and assumptions are given on page 11. We repeat the perturbation model:

$$R_{\text{in}} = R_I \qquad R_{\text{out}}(\theta) = R_{II} + \varepsilon \cdot \cos\theta \ .$$

The outer conductor need not be considered, because the current densities are assumed not to vary with θ.

We take the following 'Ansatz' for the magnetic potential:

$$A(r, \theta) = \alpha_0(r) + \sum_{k=1}^{\infty} [\alpha_k(r) \cos k\theta + \beta_k(r) \sin k\theta] \ ,$$

which happens to simplify to

$$A(r, \theta) = \alpha_0(r) + \alpha_1(r) \cos\theta$$

because

- sine components are to be ruled out because of the problem's top–bottom symmetry;
- higher-order waves turn out to have amplitudes of only second or higher order in the disturbance parameter ε,which could already be expected from physical insight.

Thanks to the preparation work performed in Appendix A2, the solution is readily formalized in the regions of interest:

$$0 \le r \le R_{\text{in}}: \qquad A = c''_1 r \cos\theta \ , \qquad d''_0 = 0 \ ,$$
$$d''_1 = 0 \qquad \text{(avoid singularity at } r = 0) \ .$$

$$R_{\text{in}} \le r \le R_{\text{out}}: \quad A = -\frac{\mu_0 J r^2}{4} - c'_0 \ln\frac{r}{R_{II}} + d'_0 + \left(c'_1 r + \frac{d'_1}{r}\right) \cdot \cos\theta \ .$$

$$R_{\text{out}} \le r: \qquad A = -c_0 \cdot \ln\frac{r}{R_{II}} + d_0 + \left(c_1 r + \frac{d_1}{r}\right) \cdot \cos\theta \ .$$

In the last formulation, the term $c_1 r \cos\theta$ should be killed, because its magnitude would grow unbounded if the outer conductor were at infinite radius: the theory should still hold in the absence of an outer tube.

The interface conditions to be imposed are the continuity of both A and $\partial A/\partial r$ at $r = R_{\text{in}}$ and $r = R_{\text{out}}$.

Each condition again decomposes into two equations: one for the DC component and one for the cosine wave.

The manipulations involve straightforward algebra at $r = R_{\text{in}} = R_I$.

At the interface $r = R_{\text{out}}(\theta)$, first-order approximations in ε are developed, such as:

$$(R_{II} + \varepsilon\cos\theta)^2 \;=\; {R_{II}}^2 + 2\varepsilon R_{II}\cos\theta \;\;,$$

$$\ln\frac{R_{II} + \varepsilon\cos\theta}{R_{II}} \;=\; \frac{\varepsilon}{R_{II}}\cdot\cos\theta \;\;,$$

$$(R_{II} + \varepsilon\cos\theta)\cdot\cos\theta \;=\; R_{II}\cos\theta + \frac{\varepsilon}{2} \qquad \text{(discard higher spatial harmonics)} \;\;.$$

After working out, the c_0- and d_0-type constants turn out to correspond to those found in Appendix A2.

Moreover,

$$c_1' \;=\; c''_1 \;=\; \frac{\mu_0 J\varepsilon}{2} \;\;, \qquad d_1 \;=\; \frac{\mu_0 J\varepsilon {R_{II}}^2}{2} \;\;, \qquad d'_1 \;=\; 0 \;\;.$$

It should be noted that there exists a uniform vertical field in the confined air volume (Fig. 12):

$$0 \le r \le R_I \;\;: \qquad B_y \;=\; -\frac{\mu_0 J\varepsilon}{2} \;\;.$$

Writing out the potential in the tube itself,

$$R_I \le r \le R_{\text{out}} \;\;: \qquad A \;=\; \frac{\mu_0 J}{4}\cdot\left[R_I^2 - r^2 + 2R_I^2\ln\frac{r}{R_I} + 2\varepsilon r\cos\theta\right] \;\;,$$

from which the relevant flux density components

$$B_r \;=\; -\frac{\mu_0 J\varepsilon}{2}\cdot\sin\theta \;\;, \qquad B_\theta \;=\; \frac{\mu_0 J}{2}\cdot\left(r - \frac{R_I^2}{r} - \varepsilon\cos\theta\right) \;\;.$$

The force distribution is no longer uniform. It is convenient to define a force density per azimuthal radian and per unit depth:

$$\vec{F}(\theta) \;=\; (F_r, F_\theta, 0) \;=\; \int_{R_{\text{in}}}^{R_{\text{out}}} \vec{f}(r,\theta)\; r\;\mathrm{d}r$$

where $\vec{f}$ has been defined in Appendix A3.

Note that for a perfect geometry $F_r \;=\; -pR$ and $F_\theta \;=\; 0$.

After working out, and again applying first-order approximations:

$$F_r \;=\; -\frac{\mu_0 J^2 R^3\tau}{2}\cdot\left\{\tau\left(1 - \frac{\tau}{6}\right) + \eta\cos\theta\right\} \;\;, \qquad F_\theta \;=\; -\frac{\mu_0 J^2 R^3\tau}{2}\cdot\eta\sin\theta$$

in which the dimensionless disturbance parameter η is defined as:

$$\eta \;=\; (\varepsilon/R) \;\;.$$

This surprisingly elegant result can be confronted with Fig. 31.

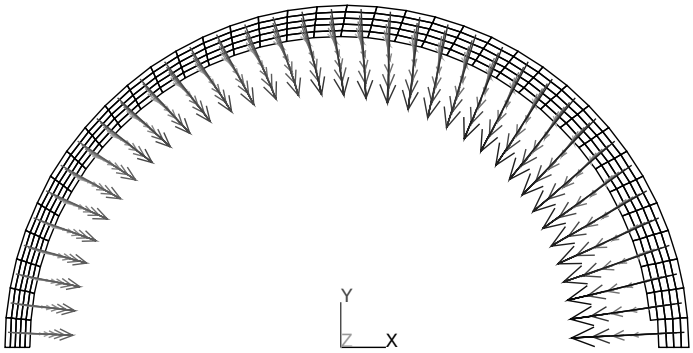

Fig. 31 Forces on a configuration with arbitrary dimensions and an exaggerated thickness variation, obtained with a finite-element test run.

The total *x* force vanishes again. More surprisingly, the bending moment turns out to be zero everywhere: the F_θ effect couterbalances the tendency to produce bending effects from 'pressure' (F_r) non-uniformities! Consequently, the tube happens to be loaded in pure compression, as in the unperturbed case.

Higher spatial frequency

Assumed waveform:

$$R_{\text{in}} = R_I \qquad R_{\text{out}}(\theta) = R_{II} + \varepsilon \cdot \cos 2\theta \ .$$

Potential:

$$A(r, \theta) = \alpha_0(r) + \alpha_2(r) \cos 2\theta \ .$$

Solutions written out in each region, with similar motivations to before:

$$0 \le r \le R_{\text{in}} : \qquad A = c''_2 r^2 \cos 2\theta$$

$$R_{\text{in}} \le r \le R_{\text{out}} : \qquad A = -\frac{\mu_0 J r^2}{4} - c'_0 \ln\frac{r}{R_{II}} + d'_0 + \left(c'_2 r^2 + \frac{d'_2}{r^2} \right) \cdot \cos 2\theta$$

$$R_{\text{out}} \le r : \qquad A = -c_0 \cdot \ln\frac{r}{R_{II}} + d_0 + \frac{d_2}{r^2} \cdot \cos 2\theta$$

Results of the usual manipulations, the c_0- and d_0-type constants again being unperturbed:

$$c_2' = c''_2 = \frac{\mu_0 J \varepsilon}{4 R_{II}} \ , \qquad d_2 = \frac{\mu_0 J \varepsilon R_{II}^3}{4} \ , \qquad d'_2 = 0 \ .$$

It should be noted that the field in the confined air volume can again be rationalized:

$$0 \le r \le R_I : \qquad B_x = -c''_2 \cdot y \ , \qquad B_y = -c''_2 \cdot x \ .$$

Writing out the potential in the tube itself:

$$R_I \le r \le R_{\text{out}} : \qquad A = \frac{\mu_0 J}{4} \cdot \left[R_I^2 - r^2 + 2R_I^2 \ln\frac{r}{R_I} + \frac{\varepsilon}{R_{II}} r^2 \cos 2\theta \right] ,$$

from which the relevant flux density components:

$$B_r = -\frac{\mu_0 J}{2} \cdot \frac{r}{R_{II}} \cdot \varepsilon \sin 2\theta \quad , \qquad B_\theta = \frac{\mu_0 J}{2} \cdot \left(r - \frac{R_I^2}{r} - \frac{r}{R_{II}} \varepsilon \cos 2\theta \right) .$$

Force densities:

$$F_r = -\frac{\mu_0 J^2 R^3 \tau}{2} \cdot \left\{ \tau \left(1 - \frac{\tau}{6} \right) + \frac{1 + \tau - (\tau^2/12)}{1 + (\tau/2)} \cdot \eta \cos 2\theta \right\} ,$$

$$F_\theta = -\frac{\mu_0 J^2 R^3 \tau}{2} \cdot \frac{1 + (\tau^2/4)}{1 + (\tau/2)} \cdot \eta \sin 2\theta \ .$$

As for the perfect geometry, discussed in Section 2, there remain compression effects. The tube is very stiff for this mode: the very small elastic deformations hardly need to be considered. Buckling risks of course remain a topic of interest.

The non-uniform force density however will load the tube in an additional, unfavourable mode. The tube's cross-section will be subjected to bending effects, and it will deform to some egg shape. For significant imperfection magnitudes, these bending deformations could well become a nuisance… long before reaching the instability loading limit.

There is little hope of finding elegant analytical solutions to the elastic deformation problem.

From the formula for F_r quoted above, it can be readily seen that the non-uniformity in the loading itself can become relatively important for relatively thin tube cross-sections. These are exactly the cross-sections which show low stiffness under egg-shape deformations!

So we have taken the geometry of the horn's first portion (R = 77.5 mm, t = 2 mm) as a basis for numerical computations of the nonlinear deformation behaviour.[1] The results are depicted in Figs. 32 and 33.

For those who are not familiar with elastic stability and imperfections, we can recommend the introductory chapter of Ref. [4].

1. Finite element. 90 low order, 2-node beam elements to model 90 degree arc (higher order, curved, beams were not available) — symmetry boundary conditions — nonlinearities switched on: large deflections & stress stiffening.

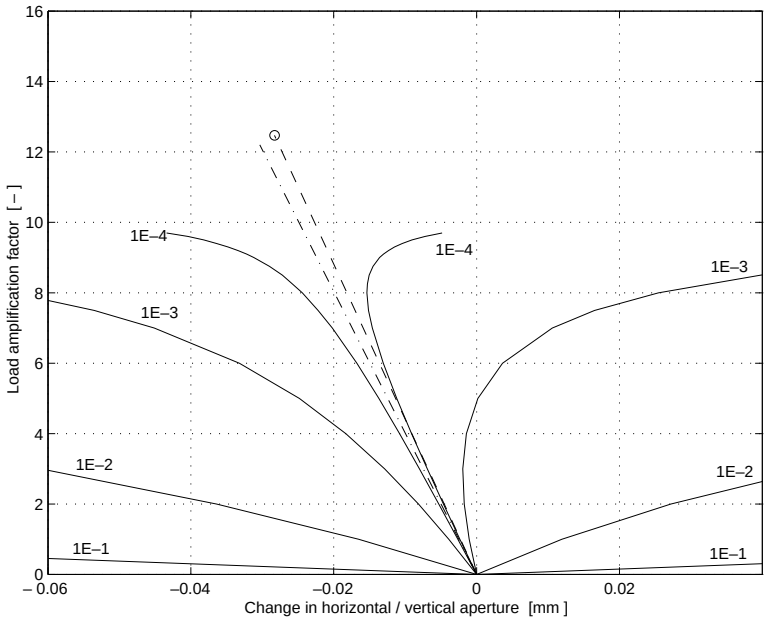

Fig. 32 Elastic deformations of a tube cross-section, represented as load-versus-deflection curves. Dashed line: perfect geometry; change in diameter; pure compression. This line ends at the bifurcation point corresponding to $p_{b,th}$ of Section 2. Solid curves show the responses of tubes with different imperfection amplitudes ε: 10^{-4}, 10^{-3}, 10^{-2} and 10^{-1} mm, respectively, from the steepest down to the flattest curve. Curves on the left-hand side of the perfect path show the change in x aperture, those on the right the change in y aperture. The dashed-dotted line is the finite element model's response with $\varepsilon = 0$. The disagreement with the 'analytical' line is not entirely understood.

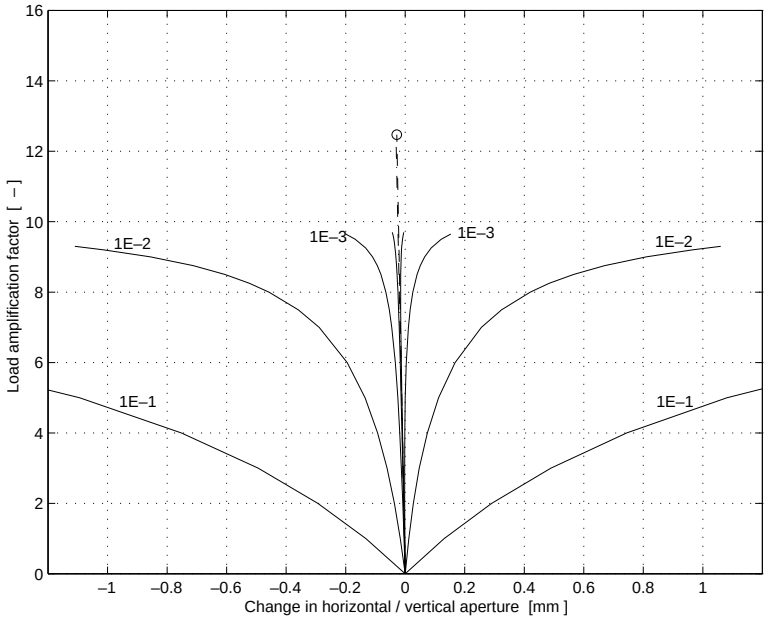

Fig. 33 The same data, on an expanded deflection scale.

The load amplification factor is a scalar scaling to the $\vec{F}$ force system. It is a mechanical scaling, so factors of 1, 4 and 9 correspond to total currents of 100, 200 and 300 kA, respectively.

The increase in stress levels because of bending can become quite significant. For instance, for a load factor of 4 and $\varepsilon = 0.1$ mm, the normal stresses are as follows.

- at $\theta = 0$: +7.0 MPa inner fibre; –14.9 MPa outer fibre
- at $\theta = \pi/2$: –16.1 MPa inner fibre; +8.4 MPa outer fibre

We conclude that there is hardly any reason for panic about an increased danger of collapse. However, the bending deformations become important even for small thickness deviations.

APPENDIX A5

UNROUNDNESS OF INNER CONDUCTOR: FIRST-ORDER PERTURBATIVE ANALYSIS

Assumed waveform:

$$R_{\text{in}}(\theta) = R_I + \varepsilon \cdot \cos 2\theta \qquad R_{\text{out}}(\theta) = R_{II} + \varepsilon \cdot \cos 2\theta \ .$$

Potential shapes are the same as on page 36. The integration constants now turn out to be

$$c'_2 = \frac{\mu_0 J \varepsilon}{4 R_{II}} \ , \qquad c''_2 = \frac{\mu_0 J \varepsilon}{4} \cdot \left(\frac{1}{R_{II}} - \frac{1}{R_I} \right) \ ,$$

$$d_2 = \frac{\mu_0 J \varepsilon}{4} \cdot \left(R_{II}^3 - R_I^3 - \frac{R_{II}^4}{R_I} \right) \ , \qquad d'_2 = - \frac{\mu_0 J \varepsilon}{4} \cdot R_I^3 \ .$$

For the field in inner space, of course with the same shape as for cos 2θ-type thickness variation, note the change of sign and the considerably lower magnitude; compare Fig. 14 with Fig. 16. In the case of unroundness, the impact is apparently smaller.

Potential in the tube's material:

$$R_{\text{in}} \le r \le R_{\text{out}} \ : \qquad A = \frac{\mu_0 J}{4} \cdot \left[R_I^2 - r^2 + 2 R_I^2 \ln \frac{r}{R_I} + \left(\frac{r^2}{R_{II}} - \frac{R_I^3}{r^2} \right) \varepsilon \cos 2\theta \right] \ .$$

Resulting force densities:

$$F_r = C \cdot \{ \ G_r(\tau) + H_r(\tau) \cdot \eta \cos 2\theta \ \} \ , \qquad F_\theta = C \cdot H_\theta(\tau) \cdot \eta \sin 2\theta \ ,$$

in which

$$C = - \frac{\mu_0 J^2 R^3 \tau^2}{2} \cdot \left(1 - \frac{\tau}{6} \right) \ ,$$

$$G_r(\tau) = 1 \ , \qquad H_r(\tau) = \frac{2}{1 + \frac{\tau}{2}} \ , \qquad H_\theta(\tau) = \frac{1}{1 + \frac{\tau}{2}} \ .$$

It will be noted that the force system tries to stabilize the geometry, tending to make the imperfection disappear.

The reader is invited to compare the τ^2 dependence (approximately) here with the τ dependence in Appendix A4. This is yet another indication that unroundness gives only a small force effect.

Analytical expressions for the elastic cross-section deformation can be found. We make the following assumptions:

- the tube's wall is thin;
- deformations due to compression and due to shear are neglected, only bending being considered;
- we again develop first-order approximations in ε.

Our analytical developments have so far been on a per unit depth *(z)* basis. This will continue to be the case, and thus the cross-section will be regarded as a bending beam, closed on itself.

Deflections of curved beams can conveniently be computed with Castigliano's theorem, of course under the assumption of linear behaviour.

In concrete terms, if we want the change in horizontal aperture, it is necessary to

- Support the tube at 9 o'clock, and monitor the deflection u_x of the 3 o'clock position. This gives a clear problem specification and avoids errors of a factor 2.
- Apply a dummy load according to the specific deflection degree of freedom. So in our case, the dummy load would be a force F_x at 3 o'clock.
- Compute the bending moment profile due to the dummy load:

$$M_{b,\,dummy}(\theta) = \alpha \cdot F_x \ ,$$

  explicitly demonstrating linearity.
- Compute the bending moment due to the actual load:

$$M_{b,\,nom}(\theta) = \beta \cdot (\text{the } F \text{ system}) \ .$$

- Evaluate the total elastic energy (strain energy):

$$U = \int \frac{M_{b,\,tot}^2}{2EI_b}\,\mathrm{d}s \ ,$$

  in which

$$M_{b,\,tot} = M_{b,\,dummy} + M_{b,\,nom} = \alpha F_x + \beta F \ ,$$

$$I_b = \frac{t^3}{12(1-\nu^2)} \ ,$$

  and where $\mathrm{d}s$ is a line element along the beam's neutral fibre.

  We repeat that forces and bending moments are per unit depth.

  Now, according to Castigliano's theorem,

$$u_x = \left.\frac{\partial U}{\partial F_x}\right|_{F_x = 0} \ .$$

  The order of differentiation and integration may be inversed. With

$$\frac{\partial}{\partial F_x}\left(\frac{M_{b,\,tot}^2}{2}\right) = \alpha \cdot (\alpha F_x + \beta F)$$

one finds

$$u_x = \frac{1}{EI_b} \cdot \int \alpha \cdot \beta F \,\mathrm{d}s \ .$$

For our perturbed geometry,

$$\mathrm{d}s = [r(\theta) + O(\varepsilon^2)] \cdot \mathrm{d}\theta \ ,$$

r being the instantaneous, radial position of the neutral fibre, yielding the final recipe:

$$u_x = \frac{2}{EI_b} \cdot \int_0^{\pi} \alpha \, M_{b,\,nom} \, r \, \mathrm{d}\theta \ .$$

Working out bending moment profile expressions, on a curved beam, closed on itself, is a tedious undertaking.

We only quote the end results. The bending moments are taken to be positive when they tend to stretch the outer fibres.

Bending moment due to dummy-load, influence coefficient:

$$\alpha(\theta) = A_0 + A_1 \sin\theta + A_3 \sin 3\theta \qquad \text{for} \quad 0 \le \theta \le \pi \ ,$$

$$\alpha(\theta) = A_0 - A_1 \sin\theta - A_3 \sin 3\theta \qquad \text{for} \quad \pi \le \theta \le 2\pi \ ,$$

in which

$$A_0 = \frac{R}{\pi} - \frac{2\varepsilon}{3\pi} \ , \qquad A_1 = -\frac{R}{2} + \frac{\varepsilon}{4} \ , \qquad A_3 = -\frac{\varepsilon}{4} \ .$$

The reader is invited to check the required left/right and top/bottom symmetries, and to note that the kinks in the profile at 9 and 3 o'clock are consistent with the occurrence of discrete forces there.

Bending moment due to actual load:

$$M_{b,\,nom}(\theta) = C \, R \cdot \left(-G_r + \frac{1}{3} H_r - \frac{1}{6} H_\theta \right) \cdot \eta \, \cos 2\theta \ .$$

Finally, the wanted deflection is equal to the increase in horizontal aperture:

$$u_x = \frac{2CR^3}{3EI_b} \cdot \left(-G_r + \frac{1}{3} H_r - \frac{1}{6} H_\theta \right) \cdot \eta = \frac{8C(1-\nu^2)}{E\tau^3} \cdot \left(-G_r + \frac{1}{3} H_r - \frac{1}{6} H_\theta \right) \cdot \eta \ .$$

Lots of terms could be discarded because they were of higher order in ε. Thanks to this, the end result can still be overlooked. Figure 34 serves as an extra aid.

So, roughly:

$$u_x \approx -\frac{4C}{E\tau^3} \cdot \eta \ .$$

In order to get some feeling about values, we test again the most vulnerable region, i.e. the entrance portion (R = 77.5 mm, t = 2 mm). Figure 35 depicts the analytical result, again as a function of a load amplification, as well as the outcome of nonlinear FE work. Neither of the two developments consider the change in magnetic field due to elastic deformations of the conductor, another stabilizing effect. So, whenever the plotted deflection becomes significant with respect to 2ε, the results lose validity.

The very obvious conclusion is that unroundness is not a topic of great concern.

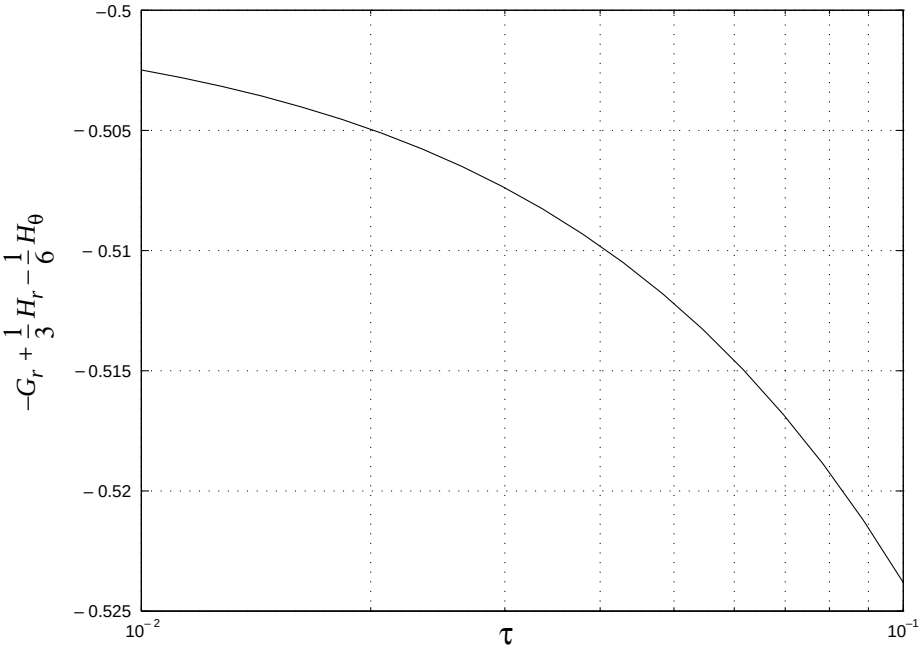

Fig. 34 A mysterious factor, occurring in bending moment and deflection expressions, mildly varying with thickness ratio. One should keep in mind that the theory loses its validity for higher τ.

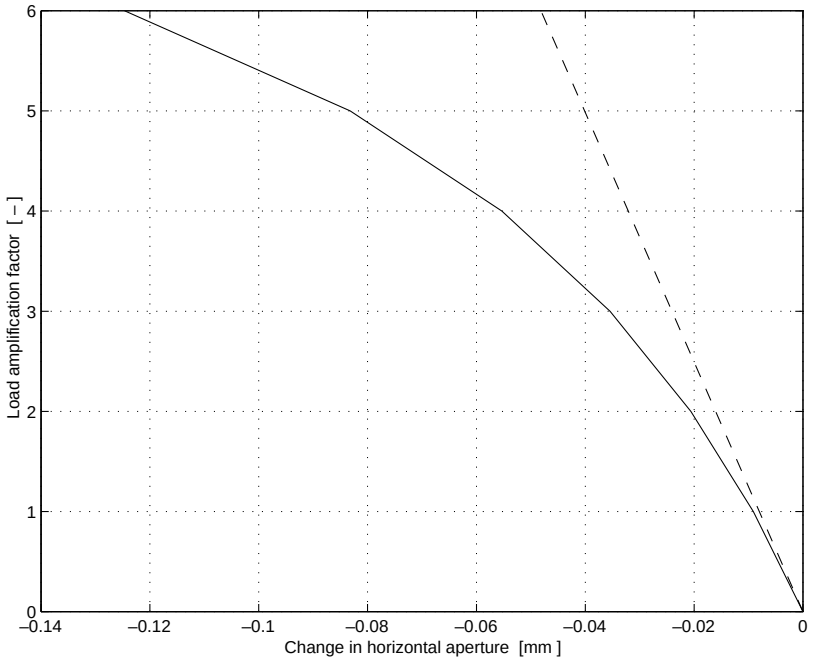

Fig. 35 Elastic deformations: change in x aperture for a scaled load system (ε = 0.1 mm). Dashed: analytical, only bending effects. Solid: finite element, bending and compression, nonlinear.